Mon. Not. R. Astron. Soc. **000**, 000–000 (0000) Printed 5 February 2008 (MN LATEX style file v2.2)

The Rest-frame Optical Colors of 99,000 SDSS Galaxies

V. Smolčić[1,2,3], Ž. Ivezić[4,1], M. Gaćeša[2,5], K. Rakos[6], K. Pavlovski[2], S. Ilijić[7], M. Obrić[8,4], R.H. Lupton[1], D. Schlegel[1], G. Kauffmann[9], C. Tremonti[10], J. Brinchmann[9], S. Charlot[9], T.M. Heckman[11], G.R. Knapp[1], J.E. Gunn[1], J. Brinkmann[12], I. Csabai[13], M. Fukugita[14], J. Loveday[15]

[1] *Princeton University Observatory, Peyton Hall, Princeton NJ 08544-1001, USA*
[2] *University of Zagreb, Physics Department, Bijenička cesta 32, 10000 Zagreb, Croatia*
[3] *Max Planck Institut für Astronomie, Königstuhl 17, Heidelberg, D-69117, Germany*
[4] *Department of Astronomy, University of Washington, Box 351580, Seattle, WA 98195-1580, USA*
[5] *University of Connecticut, Physics Department, 2152 Hillside Road, Storrs, CT 06269-3046, USA*
[6] *Institut für Astronomie, Universität Wien, Türkenschanstrasse 17, A-1180 Wien, Austria*
[7] *Faculty of Electrical Engineering and Computing, Unska 3, 10000 Zagreb, Croatia*
[8] *Kapteyn Astronomical Institute, University of Groningen, P.O.BOX 800, 9700AV Groningen, The Netherlands*
[9] *Max-Planck-Institute für Astrophysik, D-85748, Garching, Germany*
[10] *Hubble Fellow, University of Arizona, Steward Observatory, 933 N. Cherry Ave., Tucson, AZ 85721, USA*
[11] *Department of Physics & Astronomy, Johns Hopkins University, Baltimore, MD 21218, USA*
[12] *Apache Point Observatory, 2001 Apache Point Road, P.O. Box 59, Sunspot, NM 88349-0059, USA*
[13] *Department of Physics, Eötvös University, Postfach 32, Budapest H-1518, Hungary*
[14] *Institute for Cosmic Ray Research, University of Tokyo, 5-1-5 Kashiwa, Kashiwa City, Chiba 277-8582, Japan*
[15] *Astronomy Centre, University of Sussex, Falmer, Brighton, BN1 9QJ*

5 February 2008

ABSTRACT

We discuss the colors of 99,088 galaxies selected from the Sloan Digital Sky Survey Data Release 1 "main" spectroscopic sample (a flux limited sample, $r_{Pet} < 17.77$, for 1360 deg^2) in the rest-frame Strömgren system (*uz*, *vz*, *bz*, *yz*). This narrow-band ($\sim$200 Å) photometric system, first designed for the determination of effective temperature, metallicity and gravity of stars, measures the continuum spectral slope of galaxies in the rest-frame 3200–5800 Å wavelength range. We synthesize rest-frame Strömgren magnitudes from SDSS spectra, and find that galaxies form a remarkably narrow locus ($\sim$0.03 mag) in the resulting color-color diagram. Using the Bruzual & Charlot population synthesis models, we demonstrate that the position of a galaxy along this locus is controlled by metallicity and age of the dominant stellar population. The distribution of galaxies along the locus is bimodal, with the local minimum corresponding to an $\sim$1 Gyr old single stellar population. The position of a galaxy perpendicular to the locus is independent of metallicity and age, and reflects the galaxy's dust content, as implied by both the models and the statistics of IRAS detections.

Comparison of the galaxy locus in the rest-frame Strömgren color-color diagram with the galaxy locus in the H_δ-$D_n(4000)$ diagram, utilized by Kauffmann et al. (2003) to estimate stellar masses, reveals a tight correlation, although the two analyzed spectral ranges barely overlap. Furthermore, the rest-frame $r-i$ color (5500–8500 Å wavelength range) can be "predicted" with an rms of 0.05 mag using the rest-frame Strömgren colors. *Overall, the galaxy spectral energy distribution in the entire UV to near-IR range can be described as a single-parameter family with an accuracy of 0.1 mag, or better.* This nearly one-dimensional distribution of galaxies in the multi-dimensional space of measured parameters strongly supports the conclusion of Yip et al. (2004), based on a principal component analysis, that SDSS galaxy spectra can be described by a small number of eigenspectra. Furthermore, the rest-frame Strömgren colors correlate tightly with the classification scheme proposed by Yip et al. (2004) based on the first three eigenspectra. Apparently, the contributions of stellar populations that dominate the optical emission from galaxies are combined in a simple and well-defined way. We also find a remarkably tight correlation between the rest-frame Strömgren colors of emission-line galaxies and their position in the Baldwin-Phillips-Terlevich diagram. These correlations between colors and various spectroscopic diagnostic parameters support earlier suggestions that rest-frame Strömgren photometry offers an efficient tool to study faint cluster galaxies and low surface brightness objects without performing time-consuming spectral observations.

Key words: methods: statistical – surveys – galaxies: fundamental parameters –

1 INTRODUCTION

The studies of galaxies have been recently invigorated due to the advent of modern sensitive large-area surveys across a wide wavelength range. The Sloan Digital Sky Survey (SDSS, York et al. 2000, Stoughton et al. 2002, Abazajian et al. 2003) stands out among these surveys because it has already provided UV to near-IR five-color imaging data, and high-quality spectra for over 100,000 galaxies. The spectroscopic galaxy sample is defined by a simple flux limit (Strauss et al. 2002), and will eventually include close to 1,000,000 galaxies.

A number of detailed galaxy studies based on SDSS data have already been published. Strateva et al. (2001) and Shimasaku et al. (2001) demonstrated a tight correlation between the $u-r$ color, concentration of the galaxy's light profile as measured by the SDSS photometric pipeline *photo* (Lupton et al. 2002), and morphology. Blanton et al. (2001) presented the SDSS galaxy luminosity function, and Kauffmann et al. (2003ab) determined and analyzed stellar masses and star-formation histories for 100,000 SDSS galaxies. A large number of other, published and ongoing, studies are based on the rich dataset provided by SDSS.

SDSS galaxy spectra have high quality (R∼1800, 3800-9200 Å wavelength range, spectrophotometric calibration better than 10%; for more details see Stoughton et al. 2002), and have been used in a number of detailed investigations, including studies of elliptical (Eisenstein et al. 2003, Bernardi et al. 2003abcd), star-forming (Hopkins et al. 2003), and active galaxies (Kauffmann et al. 2003c, Hao et al. 2005ab, Zakamska et al. 2003, 2004). Yip et al. (2004) analyzed the SDSS spectra of 170,000 galaxies using principal component analysis (Karhunen-Loéve transform). They demonstrated that SDSS galaxy spectra can be described by a small number of eigenspectra: more than 99% of the galaxies are found on a two-dimensional locus in the space spanned by the ratios of the first three eigencoefficients. Even the most extreme emission-line spectra can be described to within the measurement noise with only 8 eigenspectra. An efficient *single-parameter* classification scheme is proposed, and it suggests three major galaxy classes. Another remarkable result of their analysis is a strong correlation between various spectral lines, encoded in, and readily discernible from the eigenspectra.

It is not yet known what the results of Yip et al. imply for the detailed distribution of galaxies in color space, but it is obvious that a high degree of structure should exist. Also, a strong correlation is expected between colors and various spectroscopic parameters, such as the strength of the H_δ line and the 4000 Å break, that were recently utilized by Kauffmann et al. (2003a) to estimate stellar masses and the the dust content for SDSS galaxies.

The main goal of this paper is to investigate whether the intrinsic simplicity of galaxy spectra implied by the results of Yip et al. can be reproduced in rest-frame color-color diagrams, and whether the position of a galaxy in these diagrams is related to parameters discussed by Kauffmann et al. (2003a). We present an analysis of correlations between colors and various spectroscopic diagnostic parameters, including model-dependent estimates of stellar masses and dust content. We utilize the "rest-frame" Strömgren photometric system that measures the continuum spectral slope of galaxies in the rest-frame 3200–5800 Å wavelength range. In principle, any set of bandpasses could be used to synthesize the colors. An additional motivation for synthesizing galaxy colors in the rest-frame Strömgren photometric system is a suggestion that it is an efficient tool for studying faint cluster galaxies and low surface-brightness objects without performing time-consuming spectral observations[1] (Fiala, Rakos & Stockton 1986). The unprecedented number of high-quality SDSS spectra can be used to analyze in detail the advantages and limitations of that method, and relate galaxy colors in the Strömgren system to parameters commonly measured using SDSS data.

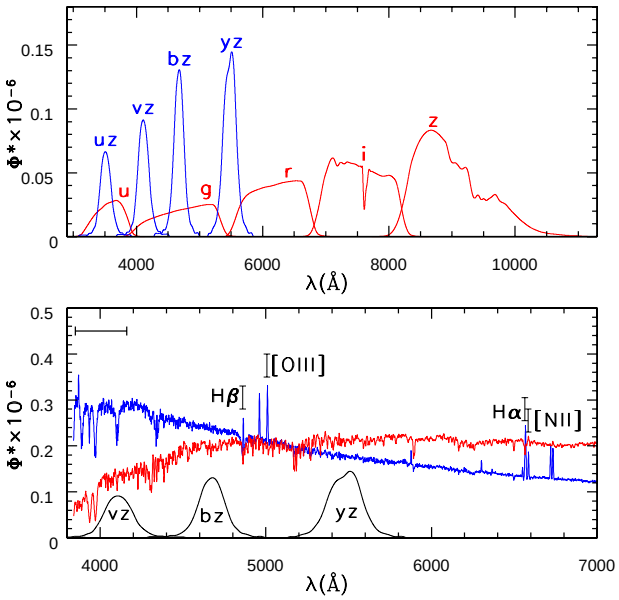

Figure 1. The top panel shows renormalized (see eq. 3) filter transmission curves for the SDSS photometric system (ugriz), and for the Strömgren photometric system. The bottom panel emphasizes the 3800-7000 Å region. The two spectra are typical for blue and red galaxies, and the four labeled emission lines are used to separate star-forming from AGN galaxies. The horizontal bar in the top left corner marks the wavelength region used in the analysis by Kauffmann et al. (2003).

We describe the synthesis of rest-frame Strömgren magnitudes from SDSS spectra in Section 2. In Section 3 we analyze the distribution of galaxies in the resulting color-color diagram, and interpret it using the Bruzual & Charlot (1993, 2003) population synthesis models. In Section 4 we demonstrate and study in detail correlations between rest-frame Strömgren colors and various diagnostic spectroscopic parameters. In Section 5 we correlate the rest-frame Strömgren colors with the spectral eigencoefficients. In Section 6 we study the properties of the galaxies at sufficiently large redshifts ($\gtrsim 0.18$) to have reliable synthesized *uz* magnitudes. We discuss and summarize our results in Section 7.

[1] Observations in the rest-frame Strömgren photometric system use filters adjusted (in hardware) to the known cluster redshift (say, from the brightest cluster galaxy).

2 THE SYNTHESIS OF REST-FRAME STRÖMGREN PHOTOMETRY

2.1 The Strömgren Photometric System

The Strömgren *uvby* narrow-band (∼200 Å) filter system was designed for measuring the temperature, chemical composition and surface gravity of stars, without resorting to spectroscopy (Strömgren 1966, for a recent compilation of over 100,000 measurements for ∼63,000 stars see Hauck & Mermilliod 1998). The bandpasses bracket the 4000 Å break and cover three regions in the 3200-5800 Å spectral region, which makes it a powerful tool for investigating stellar populations in star clusters, or composite systems such as galaxies.

The filter system used here (*uz*, *vz*, *bz*, *yz*; see next Section for details) is a somewhat modified Strömgren system, such that the filters are slightly narrower, and the filter response curves are more symmetric, than in the original system (Odell et al. 2002). The system characteristics are (see Fig. 1):

- The *uz* filter (λ_{eff} = 3500 Å) is shortward from the Balmer discontinuity (4000 $\AA$ break), and provides a measure of hot stars due to recent star formation.
- The *vz* filter (λ_{eff} = 4100 Å) extends bluewards from 4600 $\AA$, but redwards from the Balmer discontinuity. This wavelength region is strongly influenced by metal absorption lines, particularly for spectral classes F and M which typically dominate the galaxy light. The $uz - vz$ color is a good measure of the 4000 Å break.
- The *bz* (λ_{eff} = 4675 Å) and *yz* (λ_{eff} = 5500 Å) filters extend redwards from 4600 $\AA$, where the influence of absorption lines is small. The $bz - yz$ color is thus a good measure of the temperature color index, practically free of metallicity and surface gravity effects. For old stellar populations, the $vz - yz$ and $bz - yz$ color indices presumably serve as age and metallicity indicators.

2.2 The Rest-frame Strömgren Photometric System

The rest-frame Strömgren photometric system utilizes filters whose bandpasses are redshifted and stretched to correspond to the Strömgren bands in the rest-frame. This method, introduced by Fiala, Rakos & Stockton (1986), alleviates the need for $K-$corrections, and thus allows robust color comparison for galaxies at different redshifts. For example, Rakos & Schombert (1995) studied the color evolution of 17 clusters of galaxies spanning the redshift range from 0.2 to 0.9. They demonstrated that the colors of the red population are consistent with passive evolution models for a single stellar population which formed around $z = 5$. On the other hand, the fraction of blue cluster galaxies dramatically increases from 20% at $z = 0.4$ to 80% at $z = 0.9$. The rest-frame Strömgren photometric system also provides a good method for detecting cluster members, and enables an efficient spectrophotometric classification of galaxies (Rakos, Dominis and Steindling 2001; Rakos & Schombert 2004; and references therein).

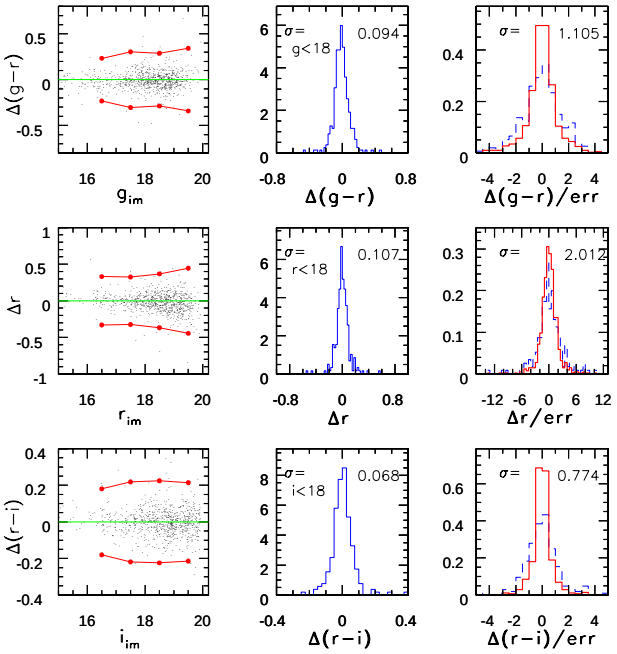

Figure 2. The comparison of imaging and synthesized SDSS magnitudes (colors) for stars, with the latter tied to imaging point-spread-function magnitudes. The first column displays the color or magnitude difference as a function of magnitude; the large symbols connected by lines show the $\pm 3\sigma$ envelope. The distribution of color or magnitude differences at the bright end is displayed in the middle column. The last column shows the

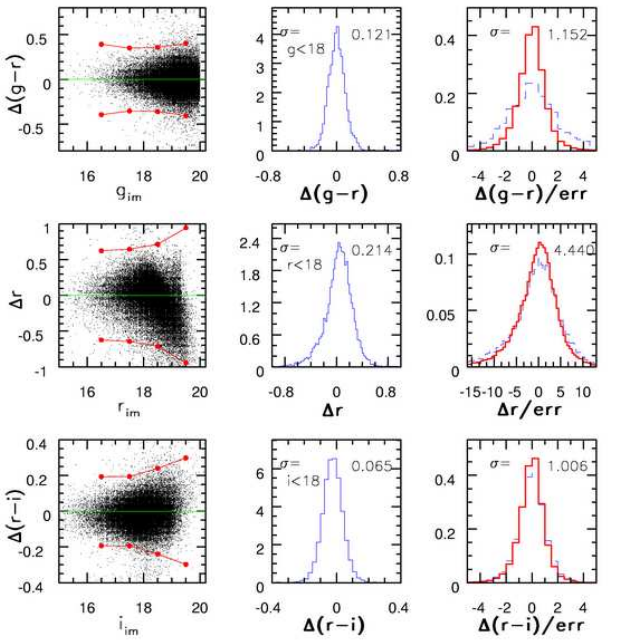

Figure 3. Analogous to Fig. 2, except that the results are shown for galaxies, and the spectrophotometric magnitudes are tied to imaging model magnitudes.

2.3 The Synthetic Strömgren Photometry from SDSS spectra

The synthetic Strömgren magnitudes are synthesized on the AB system[2] (Oke & Gunn 1983). An AB magnitude, m, in a bandpass $S(\nu)$, is defined by

$$m = -2.5 \log_{10} \frac{\int d(\log_{10} \nu) f_\nu(\nu) S(\nu)}{\int d(\log_{10} \nu) S(\nu)} - 48.6, \quad (1)$$

where f_ν is the specific flux per unit frequency (for more details see Fukugita et al. 1996). The zero-point (48.6) is chosen such that an object with a specific flux of 3631 Jy has $m = 0$ (i.e. an object with f_ν=const. has an AB magnitude equal to the Johnson V magnitude at all wavelengths). The function $S(\nu)$ includes the response of the detector, the transmissivity of the filter, the telescope, and the atmosphere of the Earth at some representative air-mass. It is convenient to express the above equation in terms of the specific flux per unit wavelength (the form used to report SDSS spectra, Stoughton et al. 2002) as

$$m = -2.5 \log_{10} \int \phi^*(\lambda) f_\lambda(\lambda) d\lambda, \quad (2)$$

where we introduced a quantity, hereafter called the *normalized filter*:

$$\phi^*(\lambda) = \frac{10^{19.44} \lambda S(\lambda)}{c \int \lambda^{-1} S(\lambda) d\lambda} \quad (3)$$

Computing m is, therefore, reduced to a simple integral of the SDSS spectrum (with the spectrum given in 10^{-17} erg/cm^2/s/Å, and λ in Å) with a *pre-computed* normalized filter. The normalized filter curves are shown in Fig. 1.

SDSS spectra are obtained using a plate with 640 spectroscopic fibers (diameter 3", corresponding to ∼6 kpc at the redshift of 0.1), which are fed to two independently calibrated spectrographs (Schlegel et al., in prep). Spectra are corrected for the Galactic interstellar dust reddening during calibration. As shown by Vanden Berk et al. (2002), the accuracy of synthesized magnitudes for point sources can be improved by requiring that the mean offset between the imaging (g, r, i) and synthesized magnitudes is zero for each spectrograph (this information is not available when calibrating spectra). We confirmed their result for point sources, and found that it also improves the synthesized photometry for galaxies (as inferred from the width of the galaxy color locus, discussed below). The synthesized photometry for galaxies can be further improved by using galaxies (instead of point sources) to correct for the mean offsets between the imaging (we use model magnitudes, see Stoughton et al. 2002 for details) and synthesized magnitudes. Hereafter, we adopt the latter method. When correcting synthesized Strömgren magnitudes, we linearly interpolate (as a function of wavelength) the g and r band corrections.

[2] Note that all the published work by Rakos and collaborators, who pioneered the redshifted Strömgren photometric system, is expressed on the Vega system.

2.4 The Tests of Synthesized Magnitudes

We synthesized SDSS magnitudes (g, r, i) and rest-frame Strömgren magnitudes (uz, vz, bz, yz)[3] for 99,088 unique "main" ($r_{Pet} < 17.77$) galaxies from SDSS Data Release 1 (Abazajian et al. 2003), as well as for stars from the same spectroscopic plates. The accuracy of synthesized magnitudes (relative to imaging magnitudes, which are accurate to 0.02 mag, Ivezić et al. 2003) for a subsample of stars is summarized in Fig. 2. The colors are reproduced with the expected accuracy (∼0.08 mag), while there are systematic errors in the overall magnitude scale at the level of 0.10 mag (root-mean-square scatter). These results are in agreement with Vanden Berk et al. (2004).

Fig. 3 summarizes the obtained accuracy for galaxies. Again, the colors are reproduced with the expected accuracy, while systematic errors in the overall magnitude scale are ∼0.2 mag. Note that using galaxies (instead of point sources) to correct for the offset between imaging and synthesized magnitudes introduces a systematic trend in the Δr distribution at the faint magnitude end. Nonetheless, as evident from the top and bottom panels, this does not significantly affect the synthetic colors as the overall trend nearly cancels out. In addition, the distribution of color-differences normalized by the expected errors (last column in Fig. 3, top and bottom panels) shows that the errors are estimated correctly (the width of the distributions is ∼1). Therefore, we do not expect this to affect the synthetic photometry significantly. The errors in rest-frame Strömgren colors are expected to be smaller than in $g - r$ and $r - i$ colors because the relevant wavelength range is shorter (and thus less sensitive to large-scale errors in the spectrophotometric calibration of SDSS spectra). We estimated errors in $vz - yz$ and $bz - yz$ colors by comparing measurements for 1253 galaxies observed twice: the scatter (root-mean-square determined from the interquartile range) for the $vz - yz$ color is 0.09 mag, and for $bz - yz$ color 0.05 mag. We tested for plate-to-plate systematics by analyzing the position of the red peak in the color distribution of galaxies (see the next Section). This position shows a scatter of ∼ 0.02 mag for $vz - yz$ color, and ∼ 0.01 mag for $bz - yz$ color. We conclude that the synthesized colors are sufficiently accurate for a detailed investigation of rest-frame colors. This is the first time that rest-frame optical colors with an accuracy of <0.1 mag are available for a sample of ∼100,000 galaxies.

3 THE COLORS OF GALAXIES IN THE REST-FRAME STRÖMGREN SYSTEM

In this Section we analyze the distribution of galaxies in the rest-frame Strömgren color-color diagram, discuss possible systematic errors and interpret the colors using model spectra.

[3] We discuss the implications of the uz magnitude separately in Section 6 since it can only be synthesized for galaxies with redshifts beyond ∼0.18.

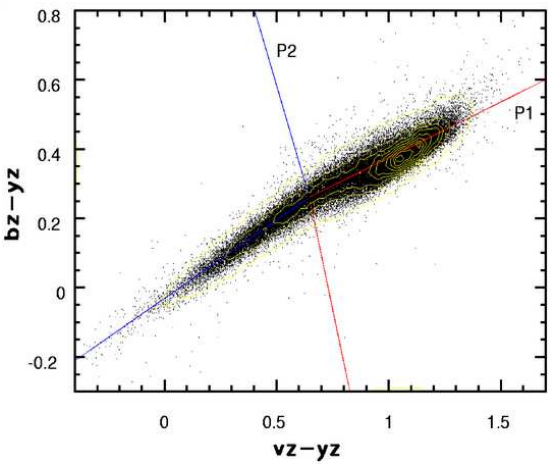

Figure 4. The distribution of 99,088 SDSS "main" galaxies in the rest-frame Strömgren color-color diagram. Each galaxy is represented by a dot, and the overall distribution is outlined by linearly spaced isopleths. The principal axes P1 and P2 are defined for the two regions separated by $vz - yz = 0.646$.

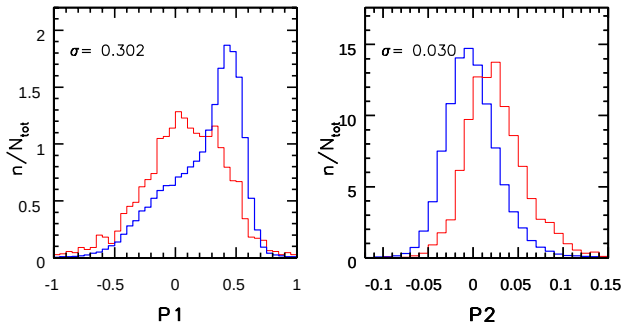

Figure 5. The color probability distributions of the principal rest-frame Strömgren colors for SDSS "main" galaxies (note different scales for x axis). The thick lines show the distributions for the whole sample, and thin lines for the subsample of galaxies detected by IRAS. The σ values shown in each panel are root-mean-square scatter (determined from the interquartile range) for the whole sample.

3.1 The Galaxy Locus and Principal Axes

The distribution of 99,088 galaxies in the rest-frame Strömgren color-color diagram is shown in Fig. 4. The distribution resembles a remarkably narrow locus. To quantify its width, we define a set of principal axes $(P1, P2)$ where $P1$ measures the position along the locus, and $P2$ perpendicular to it. Since the locus is not perfectly straight, we separately fit the blue ($vz - yz < 0.6$) and red ($vz - yz > 0.7$) ends. As the boundary between the two $(P1, P2)$ definitions we choose $vz - yz = 0.646$, where the two fits intersect. We obtain for the blue side

$$P1 = \quad 0.911\,(c_1 - 0.646) + 0.412\,(c_2 - 0.261) \qquad (4)$$

$$P2 = -0.412\,(c_1 - 0.646) + 0.911\,(c_2 - 0.261), \qquad (5)$$

and

$$P1 = \quad 0.952\,(c_1 - 0.646) + 0.307\,(c_2 - 0.261) \qquad (6)$$

$$P2 = -0.307\,(c_1 - 0.646) + 0.952\,(c_2 - 0.261), \qquad (7)$$

for the red side, with $c_1 = vz - yz$ and $c_2 = bz - yz$. The coefficients are normalized such that the errors in $P1$ and $P2$ are the same as the errors in $vz - yz$ and $bz - yz$, in the limit when the latter two are the same. It is noteworthy that the $P2$ axis is nearly parallel to the color index $m_1 = (vz - yz) - 2\,(bz - yz)$, used as a metallicity estimator for single stars (e.g. Twarog 1980).

The distributions of $P1$ and $P2$ colors are shown in Fig. 5 by thick lines. The width of the locus in the P2 direction is surprisingly small[4] (0.03 mag, and 0.32 mag in the P1 direction). Indeed, the rest-frame colors for a large number of galaxies have not been measured to date with such an accuracy. This small value both testifies that the errors in synthesized colors are small, and that *the slope of galaxy spectra in the 4000–5800 Å wavelength range is a nearly one-parameter family.*

3.2 Fiber Aperture Effects on P1 & P2

SDSS spectra are obtained with a fixed 3 arcsec diameter fiber positioned as close as possible to the center of the galaxy. Since the fiber aperture may not include the entire galaxy, it is possible that colors derived from SDSS spectra are biased red by the bulge contribution. This bias should be the largest for intermediate- and late-type galaxies where the fiber aperture may miss a significant fraction of the outer disk and its star formation. While this effect was discussed in detail elsewhere (e.g. Kauffmann et al. 2003a and Kewley et al. 2005), here we explore its impact on the P1 and P2 colors.

The fiber aperture effect will tend to make the P1 color redder for galaxies with large angular size because bulges are generally redder than disks. The expected effect for the P2 color is not so obvious. We argue below (see Section 3.4) that the P2 color is related to dust, and if this is true, the expected effect is for the P2 color to become bluer for galaxies with large angular size.

Figures 6 and 7 show the dependence of the P1 and P2 colors on the Petrosian 50% radius in the z band[5] for galaxies with the r band absolute magnitudes in the range -19 to -18. This magnitude slice is selected because it is dominated by blue galaxies where the expected effect is the strongest (see Fig. 21). As the Petrosian radius increases, the bulge contribution to the flux captured by the fiber also increases. As evident, small but measurable dependence of the P1 color on the Petrosian radius is indeed present. Given the observed range of the Petrosian radius, the expected bias in the P1 color is $\lesssim$0.05 mag, with the root-mean-square scatter contribution to the P1 measurement error of $\sim$0.02 mag. Compared to the observed P1 range, this is a small effect. The fiber aperture effect on the P2 color is entirely negligible.

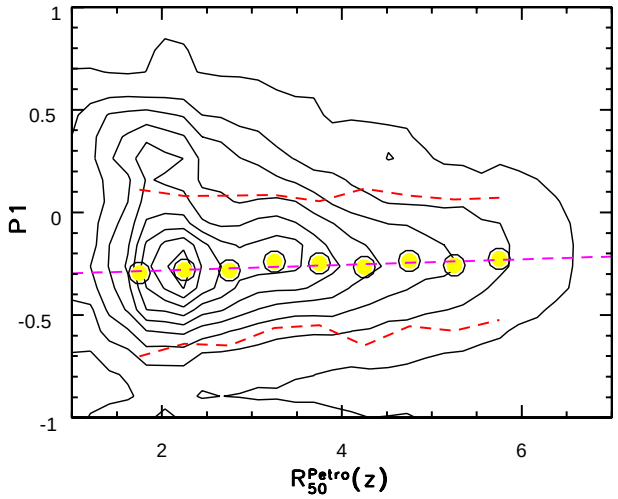

Figure 6. A test for aperture effects, due to 3 arcsec SDSS spectroscopic fiber diameter, on the P1 color. The linearly spaced contours show the distribution of galaxies with absolute Petrosian magnitude in the r band between -19 and -18 in the P1 color vs. Petrosian 50% radius in the z band (an estimator of the galaxy's size) diagram. The aperture effect is expected to be the strongest for blue galaxies with P1<0. The large circles show median P1 colors for bins of the Petrosian radius in the z band, computed for galaxies with P1<0. The middle line is a best straight line fit to these medians, and the other two lines illustrate 2σ deviation around the median. The slope of the best fit line is 0.015 mag/arcsec.

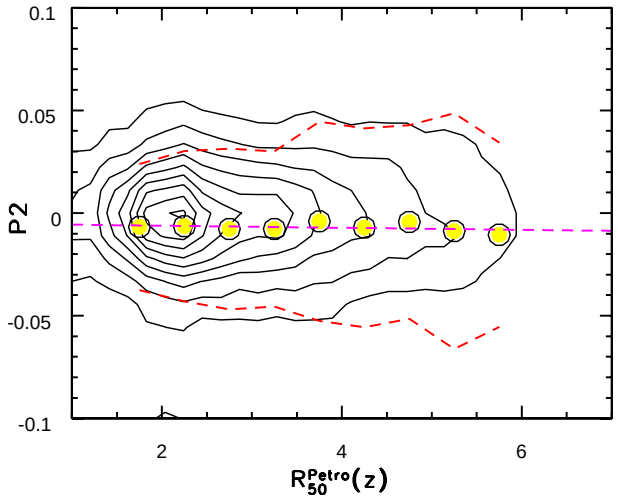

Figure 7. Analogous to Fig. 6, except for the P2 color and only for galaxies with P1<0. The slope of the best fit line is -0.0005 mag/arcsec.

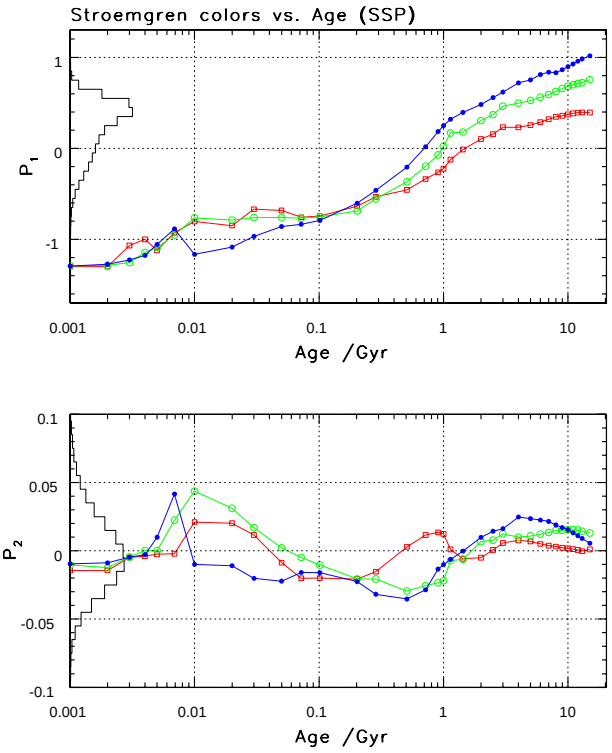

Figure 8. The Bruzual & Charlot model predictions for the dependence of the principal rest-frame Strömgren colors on the age and metallicity ([Z]=0.004, squares; 0.02, circles; 0.05, dots) of single stellar populations. Note the different scales for the two colors. The histograms on the y axes show the observed color distributions.

3.3 The Stellar Population Model Colors

The principal axes (P1,P2) are defined by the *observed* morphology of the distribution of galaxies in the rest-frame Strömgren color-color diagram. Here we relate these axes to the stellar age and metallicity using the Bruzual & Charlot (1993, 2003) population synthesis models.

Using the same method as for observed spectra, we synthesize rest-frame Strömgren colors from model spectra. Fig. 8 shows the model colors as a function of the age of a single stellar population, and for three representative metalicities. A single stellar population corresponds to a single epoch of star formation, while real galaxies likely have more complex star formation histories. In addition, for single stellar population models the star-formation rate history, which is an important discriminating parameter (e.g. Kennicutt 1998), is unavailable. Nevertheless, the color range spanned by a single stellar population provides a robust constraint on the possible color distribution for any star formation history (because it brackets the possible color range).

The observed range of the $P1$ color can be explained by stellar populations with ages from 100 Myr to 10 Gyr. Note that $P1 > 0$ corresponds to populations older than $\sim$1 Gyr,

[4] It may be surprising that the width of the P2 color distribution is smaller than the errors of the colors used to synthesize it. This is due to covariances in the $vz - yz$ and $bz - yz$ errors.
[5] For more details about the Petrosian radii see Stoughton et al. 2002, and Strauss et al. 2002.

but the age estimate is very uncertain due to the unknown metallicity.

Models provide a simple explanation for the observed small locus width: the $P2$ color is a color projection which is nearly independent of both age *and* metallicity[6]. At any age, $P2{\sim}0$ to within 0.02-0.03 mag, and for populations older than $\sim$1 Gyr, $P2{\sim}0.01$ to within 0.01 mag. That is, whatever is age or metallicity, $P2$ is always 0 to within a few hundreths of a magnitude. This is very different from $P1$ which varies by 2 magnitudes as a function of age, and up to 0.6 mag as a function of metallicity. *The ability of models to explain the mean value and the very narrow distribution of the $P2$ color is a considerable success because the principal axes $P1$ and $P2$ are defined solely by the morphology of the data distribution in the $bz-yz$ vs. $uz-yz$ color-color diagram.*

The observed width of the $P2$ distribution is wider (0.03 mag) than the model prediction ($\sim$0.01 mag). While this difference could be easily attributed to the measurement scatter or to the simplicity of the models, we find that the $P2$ color is correlated with the estimate of the galaxy dust content, A_z (the effective dust extinction in the SDSS z band), determined by Kauffmann et al. (2003a) and further discussed in Section 4.2. Hence, the larger scatter observed in the $P2$ color than predicted by the model is, at least partially, due to dust reddening (which is not included in the models).

It could be argued that the $P2-A_z$ correlation is simply due to the fact that both quantities are determined from SDSS spectra. However, they are determined using *different*, barely overlapping, spectral ranges. While Kauffmann et al. analysis utilized the 3850–4160 Å spectral range to constrain their models (and then compared imaging $g-r$ and $r-i$ colors to model-predicted colors to estimate dust reddening), $P2$ is determined from the 4000–5800 Å wavelength range (see the bottom panel in Fig. 1).

Another reasonable objection is that the A_z estimates are, of course, model dependent and consequently may not be a good measure of the dust content. However, Obrić et al. (2006) demonstrate that galaxies detected by IRAS have systematically higher values of A_z. This finding strongly suggests that A_z does provide an estimate of the dust content.

3.4 The Colors of IRAS-detected galaxies

Since the $P2-A_z$ correlation implies that $P2$ is also a measure of the galaxy dust content, galaxies detected by IRAS should have systematically higher values of $P2$. Using the same SDSS-IRAS galaxy sample discussed by Obrić et al. ($\sim$2200 probable matches for the sample of 99,088 galaxies discussed here), we compared the $P1$ and $P2$ distributions for IRAS-detected galaxies to those for the full sample. As evident from Fig. 5, galaxies detected by IRAS have systematically higher $P2$ values.

[6] The $P2$ color, while much less sensitive to metallicity than the $P1$ color, does become redder with increasing metallicity for populations older than 1 Gyr. However, the effect is exceedingly small (0.03 mag per dex). For individual stars ($P2$ is nearly parallel to m_1, c.f. section 3.1) this is large enough because their effective temperature is typically constrained much better than the star-formation history of a galaxy.

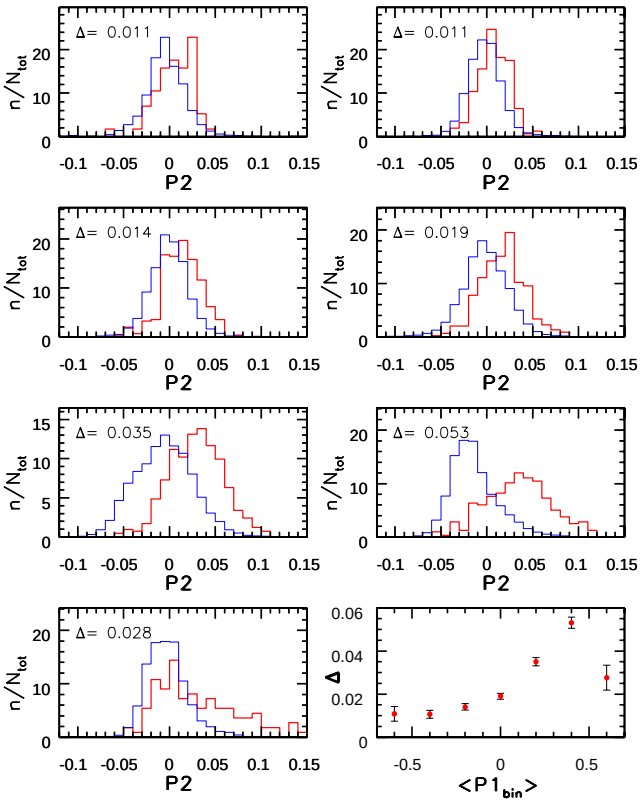

Figure 9. The comparison of $P2$ distributions for all galaxies and for the subsample detected by IRAS, for 0.2 mag wide bins in $P1$, in the range -0.7 to 0.7 (row by row, from top left to bottom right). The thin lines show the distributions for the whole sample, and the thick lines for the IRAS-detected subsample. The Δ values shown in each panel are the difference between the medians for the two distributions, and are also shown as a function of $P1$ in the bottom right panel.

The linear definition of the principal axes $P1$ and $P2$ (eqs. [4]–[7]) is not a perfect description of the galaxy locus shown in Fig. 4 because the locus is curved. Hence, the $P2$ distribution slightly changes along the locus. Since IRAS-detected galaxies are biased towards blue galaxies, it could be that the difference in $P2$ distributions for IRAS-detected and all SDSS galaxies shown in Fig. 5 is caused by the variation of the $P2$ distribution along the locus. Fig. 9 demonstrates that this is not the case: for each segment of the locus defined by a narrow bin of $P1$, IRAS-detected galaxies have systematically higher $P2$ colors. This offset strongly suggests that $P2$ is a measure of the galaxy dust content.

The shift of the $P2$ distributions between SDSS-IRAS and all SDSS galaxies is about the same as the $P2$ distribution width, so $P2$ is a rather noisy measurement of the dust content. Nevertheless, we demonstrate below that it is sufficiently efficient to study differences in the dust content between various galaxy populations separated using emission lines.

4 THE CORRELATIONS BETWEEN THE REST-FRAME STRÖMGREN COLORS AND SPECTRAL PARAMETERS

In the previous Section we have shown the connection between the two principal rest-frame Strömgren colors and galaxy physical parameters: $P1$ depends, in a degenerate way, on stellar age and metallicity, while $P2$ is correlated with the dust content, and independent of age and metallicity. In this Section we further analyze correlations between Strömgren colors and various spectral parameters. We show that the position of an emission line galaxy in a diagram commonly used to separate star-forming from AGN galaxies is well correlated with the $P1$ color, that $P1$ and $P2$ colors are correlated with the parameters discussed by Kauffmann et al. (2003ab), and that the rest-frame $r-i$ color can be predicted to better than 0.05 mag from the $P1$ color. All these correlations suggest that galaxy spectra are simple and well-defined superpositions of stellar spectra.

4.1 The Baldwin-Phillips-Terlevich Diagram

The BPT diagram (Baldwin, Phillips and Terlevich, 1981) is a standard method for classifying emission-line galaxies as star-forming and AGN galaxies. With the advent of SDSS data, it is now possible to construct the BPT diagram for an unprecedented number of galaxies (e.g. Ivezić et al. 2002, Kauffmann et al. 2003c, Hao et al. 2005ab, Heckman et al. 2004). Obrić et al. (2006) have shown that the presence of emission lines in a galaxy's spectrum is well correlated with the $u-r$ color and the concentration index determined *solely* from the imaging data. Galaxies without emission lines tend to have larger concentration indices and redder $u-r$ colors than galaxies with emission lines. Furthermore, the distribution of emission-line galaxies in the BPT diagram is also correlated with the $u-r$ color and concentration index. Galaxies classified as star-forming have predominantly blue $u-r$ colors and small concentration indices, while AGN galaxies have redder $u-r$ colors and large concentration indices.

Here we investigate the correlation between the strength of the emission lines used to construct the BPT diagram, and rest-frame Strömgren colors. To classify a galaxy as an emission-line galaxy, we require a 3σ significant detection of H_α, H_β, $[NII]$ and $[OIII\,5007]$ lines (the line strengths are determined as described by Kauffmann et al. 2003c). The bottom panel in Fig. 10 shows the distribution of 43,281 emission-line galaxies, from the sample discussed here, in the BPT diagram. To visualize the correlation with $P1$ and $P2$ colors, the dots are two-dimensionally color coded according to their position in the $P1$-$P2$ color-color diagram shown in the top panel. *There is a strong correspondence between the position of a galaxy in the BPT diagram and its $P1$ color.* Galaxies in the "star-forming branch" with small $[NII]/H_\alpha$ ratios, for a given $[OIII\,5007]/H_\beta$ ratio, have predominantly blue $P1$ colors, while AGN galaxies have redder $P1$ colors. This correlation is further illustrated in Fig. 11. The correlation with the $P2$ color is not discernible.

In the subsequent analysis, we separate emission-line galaxies in three groups according the their position in the BPT diagram: AGNs, star-forming, and "unknown". The adopted separation boundaries are shown by the dashed

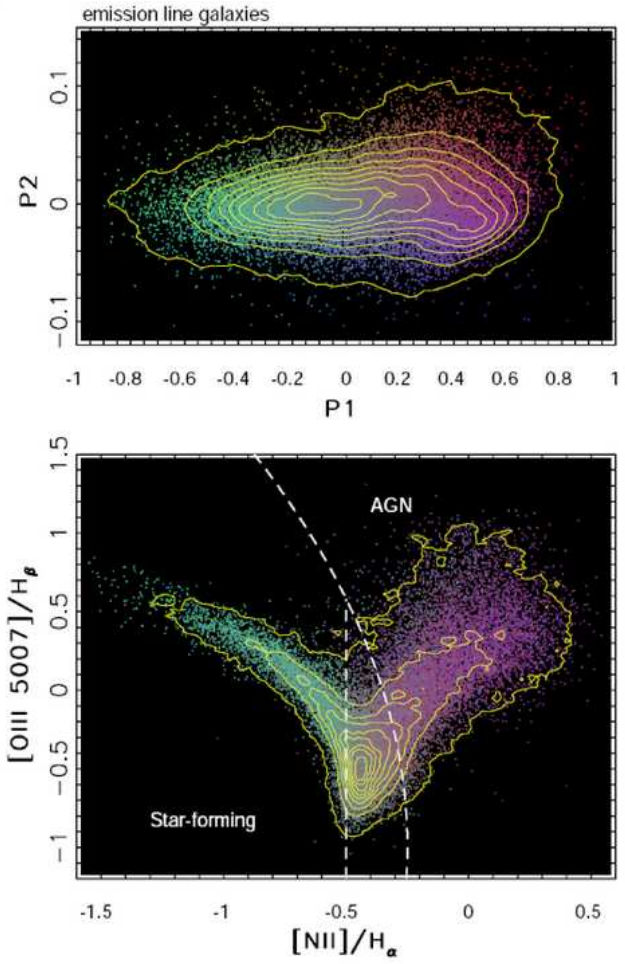

Figure 10. The top panel shows the distribution of SDSS "main" galaxies in a diagram constructed with the principal rest-frame Strömgren colors. Each dot corresponds to one galaxy; their distribution is outlined by linearly spaced isopleths. The color code is determined by the position in this diagram, and is used in subsequent figures to visualize correlations of other quantities with $P1$ and $P2$. The bottom panel shows the distribution of galaxies in the Baldwin-Phillips-Terlevich diagram, constructed with emission-line strength ratios. The dashed lines separate the regions populated by star-forming and AGN galaxies. They are motivated by the modeling results from Kewley et al. (2005) and are fine-tuned to isolate the peak of the observed distribution. For galaxies in the wedge-shaped regions the classification is uncertain. The dots are colored using $P1$ and $P2$; note the strong correlation between the $P1$ color and $[NII]/H\alpha$ ratio, although these parameters are determined in different wavelength ranges, and measure the continuum slope and line strengths, respectively.

lines. The last category is found at the joint of the two branches, and it is not obvious from the displayed data to which class these galaxies belong. Fig. 12 compares the $P1$ distributions of these classes. The majority of galaxies without emission lines and AGN galaxies have $P1 > 0$, while star-forming galaxies have $P1 < 0$. More than $\sim$2/3 of galaxies with $P1 > 0.3$ are galaxies without emission lines, and more than $\sim$2/3 of galaxies with $P1 < -0.4$ are star-forming galaxies. At least 20% of the galaxies with $P1 > 0$ harbor an AGN. The fraction of AGN galaxies drops to essentially zero by $P1 \sim -0.3$ (or by $P1 \sim -0.5$ if *all* unclassified

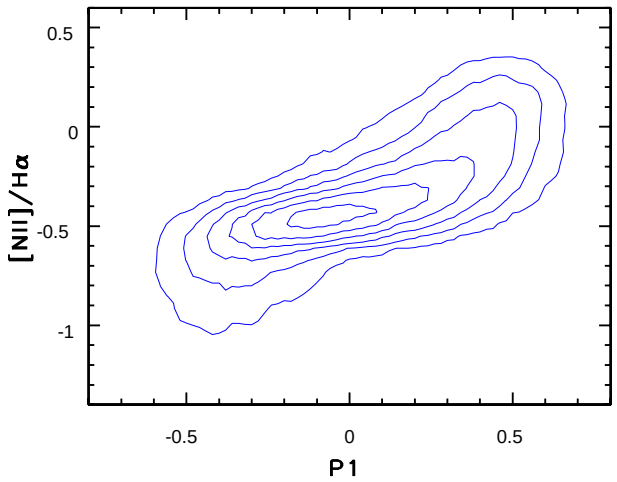

Figure 11. The correlation between the first principal axis in the rest-frame Strömgren color-color diagram, and the $[NII]/H\alpha$ line strength ratio. The distribution of all emission-line galaxies in the sample is shown by linearly spaced isopleths.

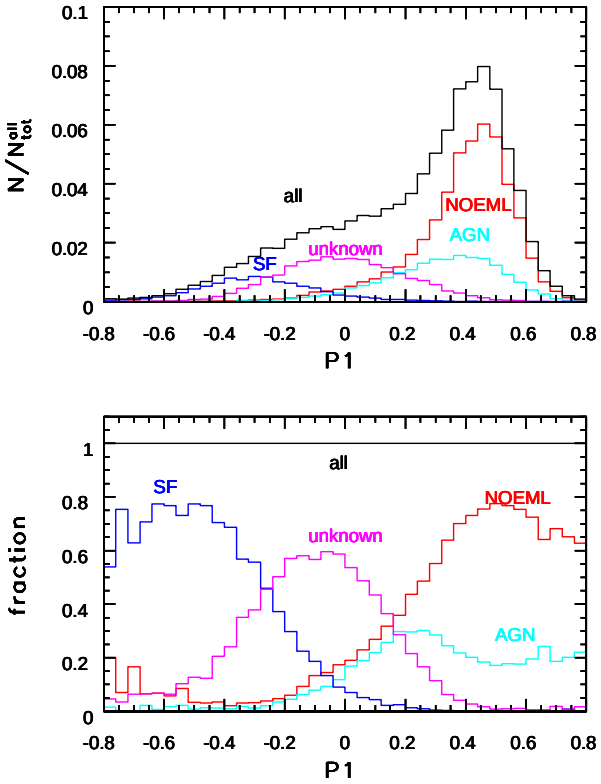

Figure 12. The distributions of $P1$, the first principal axis in the rest-frame Strömgren color-color diagram, for subsamples of galaxies separated using emission line strengths: galaxies without emission lines (NOEML), star-forming galaxies (SF), AGNs, and emission-line galaxies which cannot be reliably classified (unknown). The top panel displays counts, and the bottom panel displays the fraction of each subsample in the whole sample.

galaxies are AGNs). This dramatic absence of AGNs among the bluest galaxies appears not to be a selection effect, as discussed by Kauffmann et al. (2003c, Section 4.1).

The comparison of $P2$ distributions for the three subclasses of galaxies is shown in Fig. 13. As expected, AGNs

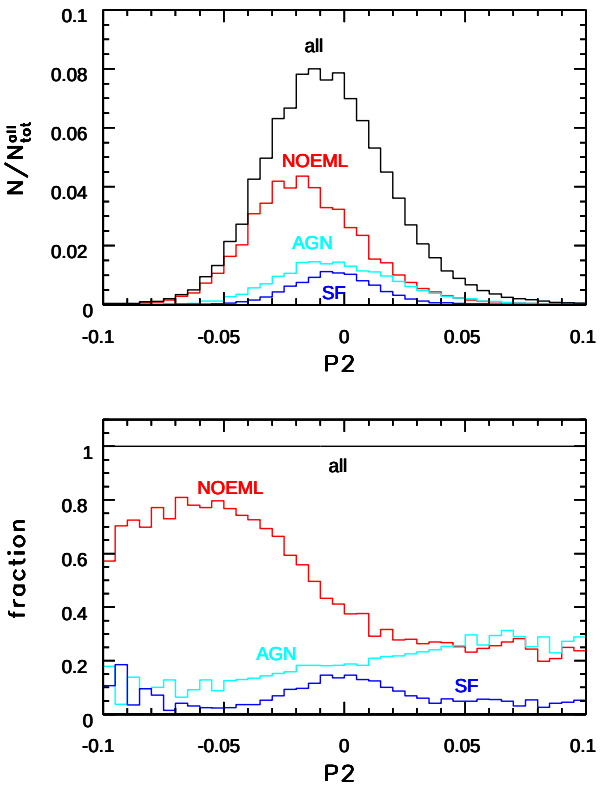

Figure 13. The distributions of $P2$, the second principal axis in the rest-frame Strömgren color-color diagram, for subsamples of galaxies separated using emission line strengths: galaxies without emission lines (NOEML), star-forming galaxies (SF) and AGNs. The top panel displays counts, and the bottom panel displays the fraction of each subsample in the whole sample (emission-line galaxies which cannot be reliably classified make up the missing fraction).

and star-forming galaxies have redder $P2$ distributions than galaxies without emission lines.

4.2 The $H_\delta - D_n(4000)$ Locus

Kauffmann et al. (2003a) used the distribution of galaxies in the plane spanned by the strength of the H_δ line and the 4000 Å break ($D_n(4000)$) to obtain model-dependent estimates of stellar masses and the dust content for SDSS galaxies. Given the position of a galaxy in the H_δ–$D_n(4000)$ plane, the most probable mass-to-light ratio is drawn from a model library. With the measured luminosity, this ratio then yields the stellar mass. The observed luminosity is corrected for the dust extinction determined by comparing observed imaging $g-r$ and $r-i$ colors to model-predicted colors (the latter do not include the effects of dust reddening). The reddening correction needed to make models agree with data is interpreted as an effective optical depth, A_z, due to the galaxy's interstellar dust. As discussed in Section 3.3, Obrić et al. (2006) demonstrate that galaxies detected by IRAS have systematically higher values of A_z, supporting the notion that A_z provides an estimate of the dust content.

The analysis by Kauffmann et al. is based on the 3850–4160 Å spectral range, marked by the horizontal bar in the

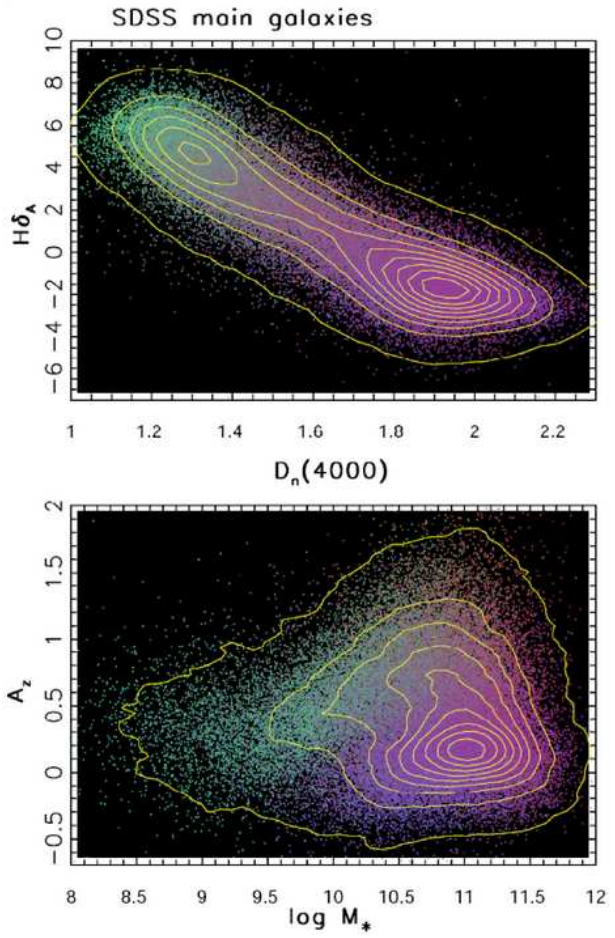

Figure 14. The top panel shows the distribution of SDSS galaxies in the plane spanned by the strength of the H_δ line and the 4000 Å break ($D_n(4000)$). Each galaxy is represented by a point color-coded according to its position in the $P1$-$P2$ color-color diagram, shown in the top panel in Fig. 10. Note the strong color gradient indicating a correlation between the position of a galaxy along this locus and its $P1$ color. The overall, strongly bimodal, distribution is outlined by linearly spaced isopleths. The bottom panel shows the distribution of the same sample in the dust content (A_z) vs. stellar mass (M_*) diagram. A_z and M_* are model-dependent estimates derived from the measured H_δ, $D_n(4000)$ and imaging $g-r$ and $r-i$ colors. The color gradients indicate good correlations between the positions in the A_z-M_* and $P1$-$P2$ planes.

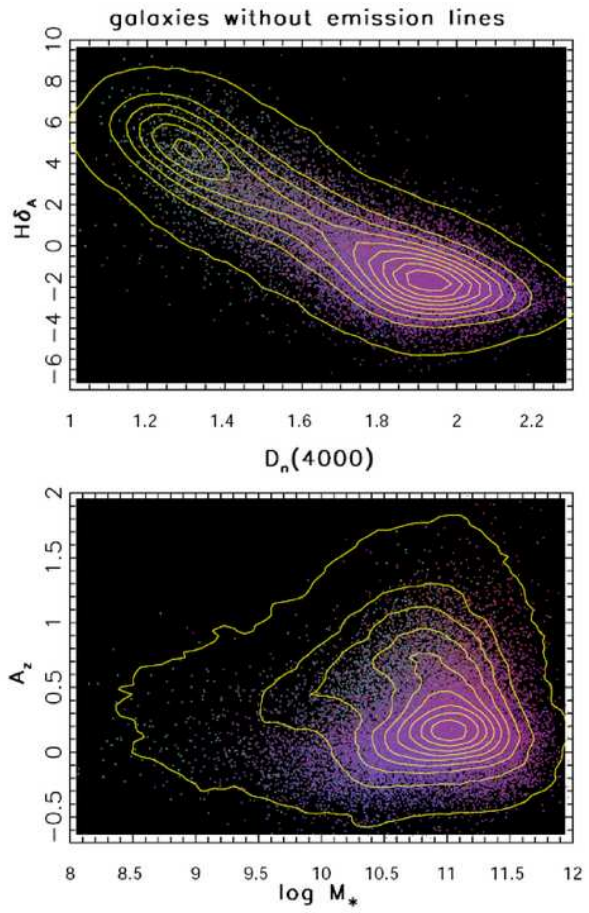

Figure 15. Analogous to Fig. 14, except that only galaxies without emission lines are shown (contours correspond to the full sample).

bottom panel in Fig. 1, while the rest-frame Strömgren colors discussed here are determined using the 4000–5800 Å range. That is, the two studies are based on practically independent spectral ranges (the vz filter does have overlap with the H_δ line). Here we demonstrate that despite their different wavelength range, and different techniques (color vs. spectral line analysis), the derived inferences about galaxies are similar.

The top panel in Fig. 14 shows the distribution of galaxies in the H_δ-$D_n(4000)$ plane, with the dots colored according to the galaxy's position in the $P1$-$P2$ color-color diagram (see the top panel in Fig. 10). As discussed by Kauffmann et al. (2003a), galaxies form a well-defined locus in this plane. The strong color gradient along the locus indicates a correlation with the $P1$ color. The bottom panel in Fig. 14 shows the distribution of galaxies in the plane spanned by the derived parameters: the dust content and the stellar mass. The color gradients indicate a good correlation between the positions in the A_z-M_* and $P1$-$P2$ planes. In particular, galaxies with small masses ($\log(M_*)\lesssim 10$) are dominated by blue galaxies with $P1 < 0$, while a correlation between A_z and $P2$ is discernible (gradient from purple to red as A_z increases) for high-mass galaxies ($\log(M_*)\sim 11$). Since emission line properties, discussed in the previous Section, correlate with $P1$ and $P2$ colors, it is expected that galaxies without emission lines, star-forming, and AGN galaxies display different distributions in these two diagrams. This is demonstrated in Figs. 15, 16, and 17. For example, the detailed morphology of the galaxy distribution shown in the bottom panel in Fig. 14 can be understood as a superposition of three dominant populations with distinctive positions, as seen in the bottom panels in Figs. 15, 16, and 17. It is noteworthy that the A_z-M_* correlation for star-forming galaxies shown in the bottom panel in Fig. 16 is consistent with a constant dust-to-stellar mass ratio for all galaxies.

In order to quantify the correlations between the po-

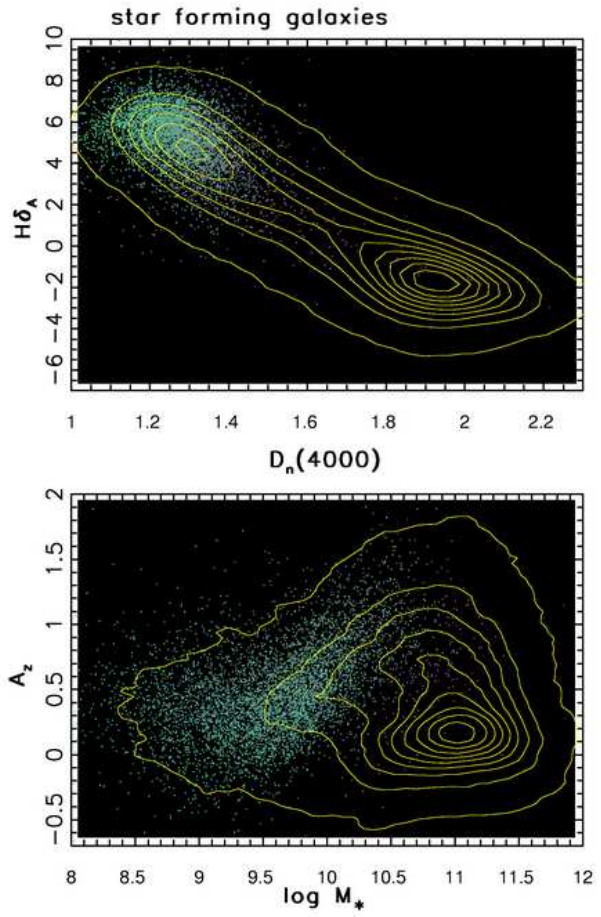

Figure 16. Analogous to Fig. 14, except that only star-formi galaxies are shown (contours correspond to the full sample).

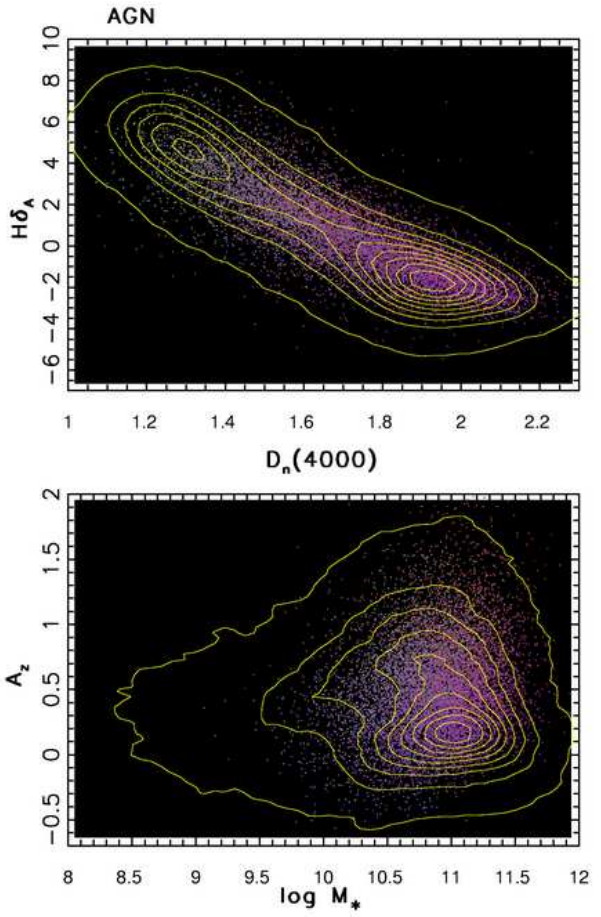

Figure 17. Analogous to Fig. 14, except that only AGN galaxies are shown (contours correspond to the full sample).

sitions in the H_δ-$D_n(4000)$ and $P1$-$P2$ planes, we define a parameter η which measures the position along the locus in the H_δ-$D_n(4000)$ plane

$$\eta = 0.0995 \cdot (D_n(4000) - 1.75) - 0.995 \cdot H\delta_A \quad (8)$$

Note that η=0 corresponds to $H\delta_A$=0. Fig. 18 compares the η-$P1$ and A_z-$P2$ distributions for galaxies with and without emission lines. As evident, there is good correspondence between the two pairs of parameters, although they are measured using barely overlapping spectral ranges. In particular, note the good correlation between A_z and $P2$ for emission line galaxies. Analogous diagrams comparing star-forming and AGN galaxies are shown in Fig. 19. It appears that the A_z-$P2$ correlation is stronger for AGN than for star-forming galaxies. This could be explained as a consequence of the more homogeneous AGN population because star-forming galaxies span a broad range in stellar mass, and hence in metallicity and surface mass density. It also seems that the slope of the A_z-$P2$ correlation is different for the two types of galaxies, but the data are too noisy to derive a robust conclusion.

4.3 The Correlations of A_z and $P2$ with the H_α/H_β Ratio

An often used estimator of the galaxy dust content is the H_α/H_β ratio. Therefore, at least some degree of correlation should exist between this parameter and the A_z and $P2$ parameters. Fig. 20 shows the dependence of $\log(H_\alpha/H_\beta)$ on $P2$ and A_z for star-forming and AGN galaxies. Similarly to A_z vs. $P2$ dependence shown in Fig. 19, it appears that different weak correlations exist for these two types of galaxies. The difference in slopes, similar to the difference in slopes for the A_z vs. $P2$ correlation, is possibly due to different dust geometries, or perhaps different dust properties, between AGN and star-forming galaxies (note that this difference also exists in the H_α/H_β vs. A_z diagram, that is, even when $P2$ is not used). A detailed analysis and interpretation of these correlations is beyond the scope of this work. We conclude that the similarity of the top and bottom panels in Fig. 20 suggests that $P2$ is a good, though somewhat noisier, proxy for A_z.

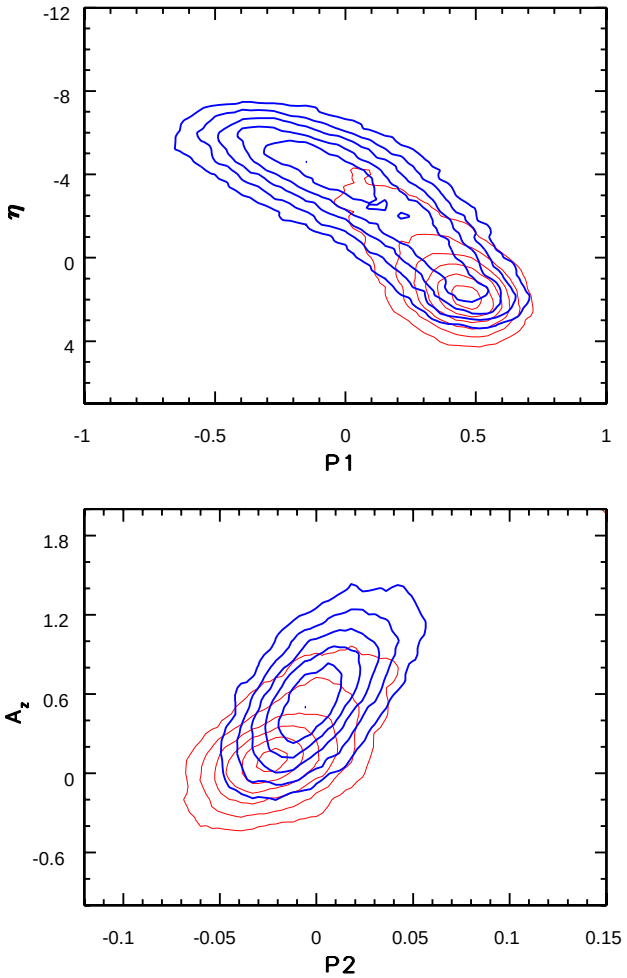

Figure 18. The top panel shows the correlation between the position of a galaxy on the locus in the H_δ-$D_n(4000)$ plane (η) and the $P1$ color. The thin contours correspond to galaxies without emission lines, and the thick contours to emission-line galaxies. The bottom panel shows the A_z-$P2$ correlation.

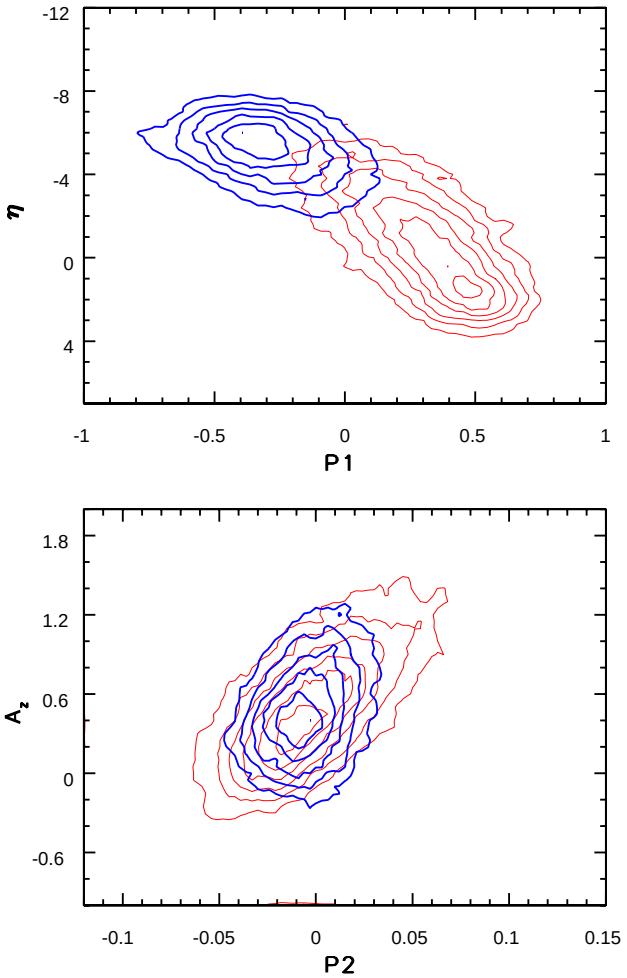

Figure 19. Analogous to Fig. 18, except that star-forming (thick contours) and AGN (thin contours) galaxies are shown.

4.4 The Color – Absolute Magnitude Distribution

The color distribution of galaxies depends on their absolute magnitude: the fraction of red galaxies increases with luminosity. Furthermore, the median color of red galaxies becomes even redder with luminosity (Baum 1959, Faber 1973). These long-known results are spectacularly confirmed by the accurate and voluminous SDSS data (e.g. Blanton et al. 2003, Baldry et al. 2004, and references therein). Hence, the distribution of the $P1$ principal color introduced here is expected to be highly correlated with luminosity.

The top panel in Fig. 21 shows the distribution of 1,704 galaxies selected from a narrow redshift range in the absolute magnitude vs. $P1$ color plane. We use the Petrosian r band magnitudes without K-correction and WMAP cosmology (Spergel et al. 2003) to compute M_{rPet} (for a description of Petrosian magnitudes see Stoughton et al. 2002, and Strauss et al. 2002). The strong color-magnitude relation for red galaxies is evident, as well as the dramatic increase in the fraction of red galaxies for $M_{rPet} < -20$. Indeed, red galaxies with $P1 \sim 0.5$ show a well-defined local maximum in their luminosity function (at $M_{rPet} \sim -20.7$).

This figure suggests that $P1 = 0.25$ provides a good separation between blue and red galaxies ($u - r = 2.22$ separator from Strateva et al. 2001 corresponds to median $P1 = 0.18$). The separation of less-luminous blue galaxies and more-luminous red galaxies is much more pronounced in this diagram based on the $P1$ color, than when using other colors such as K-corrected broad-band SDSS colors (see e.g. Fig. 7 in Blanton et al. 2003). This is presumably because $P1$ is a principal axis in a rest-frame color-color diagram constructed with narrow-band filters (the galaxy locus in the $r - i$ vs. $g - r$ rest-frame color-color diagram, discussed in Section 4.7, is twice as broad as the galaxy locus in the $bz - yz$ vs. $vz - yz$ plane).

Since the $P1$ color is correlated with numerous other parameters, the subsamples separated using those parameters should have distinct distributions in the color – absolute magnitude diagram. As an example, we choose the separation into star-forming, AGN and galaxies without emission lines. The bottom three panels in Fig. 21 compare the color–absolute magnitude distribution for each subsample to that for the full sample. As evident, AGN and galaxies without emission lines are predominantly red and luminous,

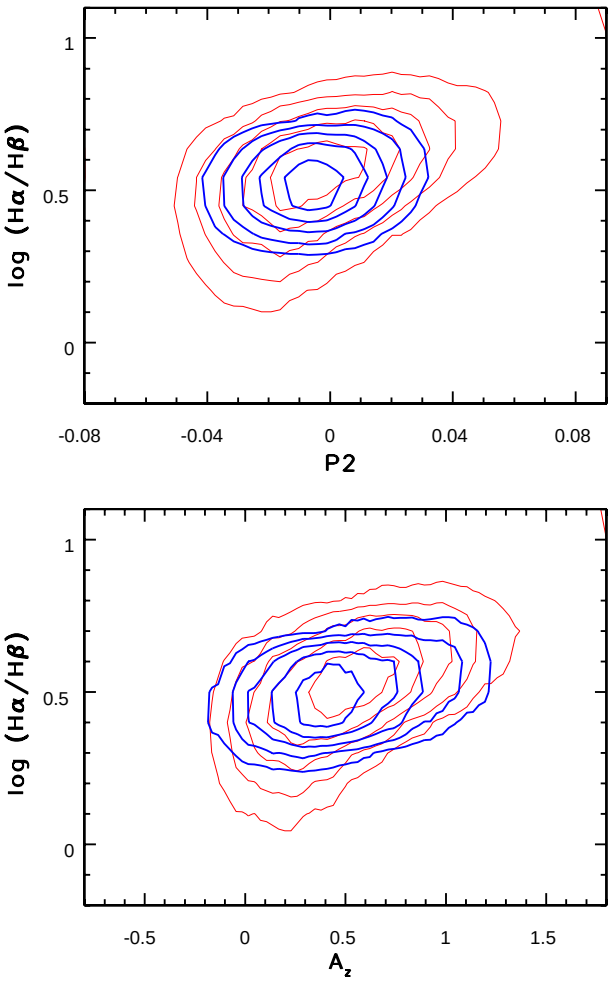

Figure 20. The comparison of $\log(H_\alpha/H_\beta)$ vs. $P2$ (top) and $\log(H_\alpha/H_\beta)$ vs. A_z (bottom) correlations for star-forming (thick contours) and AGN (thin contours) galaxies

while star-forming galaxies are blue and faint. The faint blue galaxies without emission lines, visible in the upper middle panel, are galaxies with weak emission lines that did not fulfill the condition of the 3σ detection for all four relevant emission lines.

4.5 The Color – Mass Distribution

Kauffmann et al. (2003a) estimated stellar masses for SDSS galaxies by multiplying observed luminosities (corrected for extinction using A_z) with the stellar mass-to-light ratio inferred from the position of a galaxy in the H_δ-$D_n(4000)$ plane. The correlation of the mass-to-light ratio and parameter η, which measures the position of a galaxy along the H_δ-$D_n(4000)$ locus, is shown in the top panel in Fig. 22. The dashed line is a best fit

$$\log(M/L_z) = 0.000630\eta^3 - 0.00174\eta^2 + 0.01396\eta + 0.231, \quad (9)$$

which "predicts" $\log(M/L_z)$ with an rms of 0.13 (the overall distribution of $\log(M/L_z)$ has an rms of 0.17, i.e. a factor of 1.5). The upper middle panel shows the mass-to-light ratio as a function of the $P1$ color. The best fit,

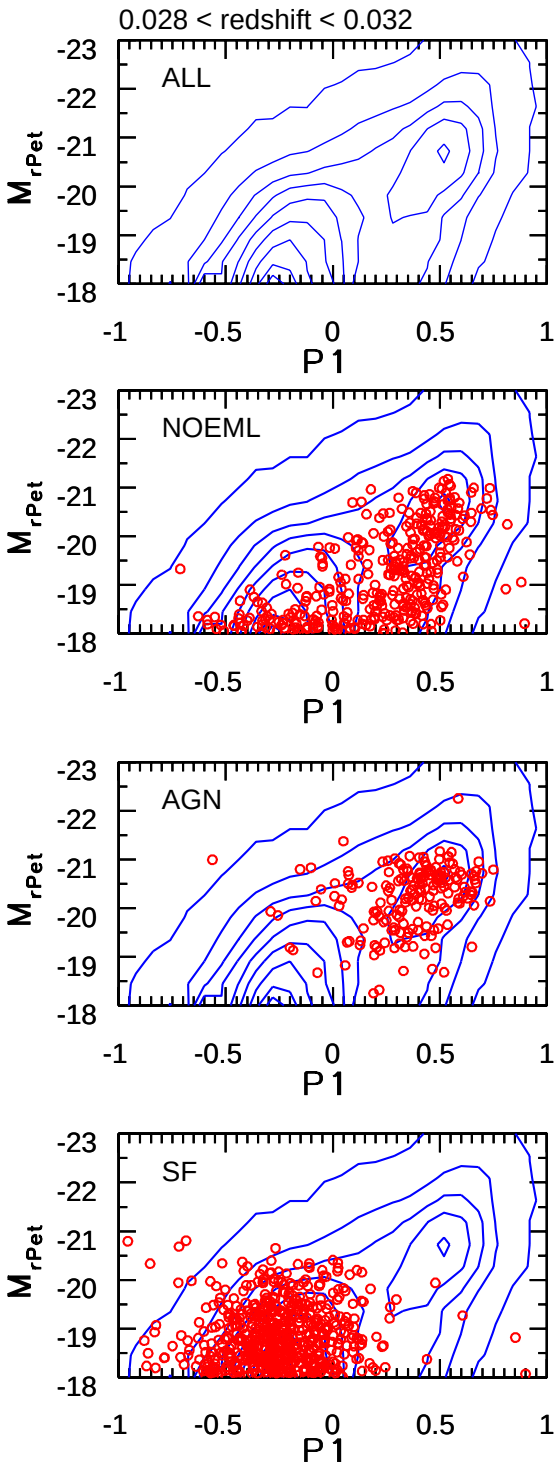

Figure 21. The color-absolute magnitude diagram for SDSS main galaxies. The top panel shows the absolute r band magnitude as a function of the P1 rest-frame Strömgren color for galaxies with 0.028<redshift<0.032. The remaining panels compare the distribution of all galaxies (contours) to the distributions of three subsamples (symbols) selected using emission lines: galaxies without emission lines in the upper middle panel, AGN galaxies in the lower middle panel, and star-forming galaxies in the bottom panel.

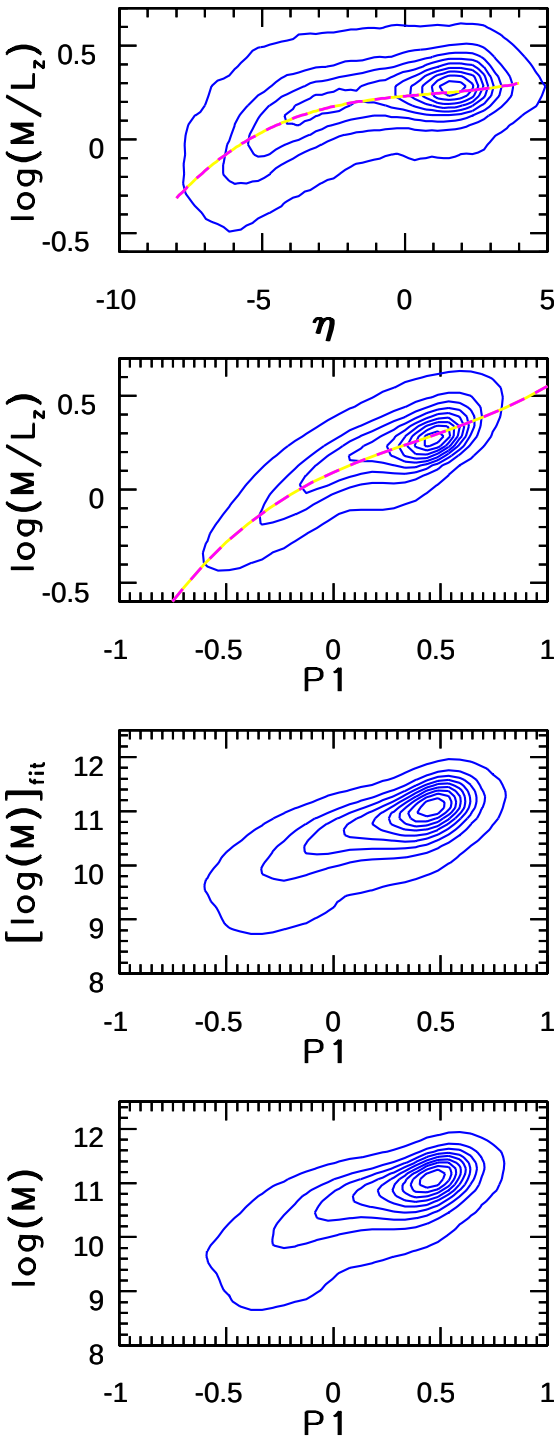

Figure 22. The top panel shows the correlation between the mass-to-light ratio (in solar units) and the position of a galaxy on the $H_\delta - D_n(4000)$ locus, where the model-dependent mass-to-light ratio is taken from Kauffmann et al. (2003). The dashed line is a best-fit third order polynomial. The upper middle panel shows the correlation between the mass-to-light ratio and the position of a galaxy on the locus in the rest-frame Strömgren color-color diagram. The dashed line is a best-fit third order polynomial. The lower middle panel shows the mass – color diagram using the best-fit mass-to-light ratio determined from the $P1$ color, and the bottom panel shows analogous distribution using the mass-to-light ratio from Kauffmann et al. (2003). Note the similarity of the two distributions.

$$\log(M/L_z) = 0.273\,P1^3 - 0.328\,P1^2 + 0.516\,P1 + 0.091, \quad (10)$$

reproduces $\log(M/L_z)$ with an rms of 0.10, equal to the median error in estimating $\log(M/L_z)$ using the Kauffmann et al. (2003a) method. Hence, *it is possible to use $P1$ to convert the observed luminosities into stellar masses* with practically the same accuracy as the H_δ-$D_n(4000)$ method employed by Kauffmann et al. (2003a). The bottom two panels compare the mass-color distributions when the mass is determined using $P1$, and when the mass is taken from Kauffmann et al. (2003a); their similarity confirms this conclusion. We note that the overall appearance of the mass-color distribution, in particular, the strong correlation of mass and color, essentially reflects the distribution of galaxies in the color-luminosity diagram (because the mass-to-light ratio has a very small dynamic range).

Since $P1$ and luminosity, L_z, are correlated, as described in the previous Section, and M/L_z is a function of $P1$, M/L_z and L_z should also be correlated to at least some extent. For example, Bernardi et al. (2003b) determined that for elliptical galaxies $M/L \propto L^{0.14}$. We find that a best power-law fit for *all* galaxies is $M/L \propto L^{0.4}$. It reproduces $\log(M/L_z)$ with an rms of 0.20. Since this scatter is larger than when determining M/L from $P1$, we speculate that galaxy colors are a better indicator of the mass-to-light ratio, and that its correlation with galaxy luminosity is probably a consequence of the color-magnitude relation.

4.6 The Color – Velocity Dispersion Distribution

Stellar velocity dispersion is automatically measured for each SDSS galaxy by fitting the observed spectrum with a linear combination of galaxy template spectra broadened by a Gaussian kernel (Schlegel et al., in prep.). Detailed analysis of velocity dispersions for elliptical galaxies, as measured by SDSS, is discussed by Bernardi et al. (2003a) and Sheth et al. (2003).

We find a good correlation between the velocity dispersion and the $P1$ color, shown in the top panel in Fig. 23. The correlation is especially strong for velocity dispersions larger than the instrumental resolution of the SDSS spectra (60-70 km/s, $\log(v_{\rm disp}/100\ {\rm km/s}) \sim -0.2$). A similar correlation between the velocity dispersion and the $g-r$ color for elliptical galaxies is discussed by Bernardi et al. (2003d).

The correlation between the velocity dispersion and the $P1$ color appears to be a consequence of the good correlation between the stellar mass and the velocity dispersion, shown in the bottom panel in Fig. 23. We find that the function

$$\log(M/M_\odot) = 10.7 + 2\,\log\left(\frac{v_{\rm disp}}{100\,{\rm km/s}}\right). \quad (11)$$

provides a good description for *both* blue and red galaxies. For a constant M, in the range $10.5 < \log(M/M_\odot) < 12$, the rms scatter in the velocity dispersion is 40 km/s, independent of M. For a constant velocity dispersion, the rms scatter in $\log(M/M_\odot)$ decreases from 0.33 for $v_{\rm disp} = 100$ km/s to 0.18 for $v_{\rm disp} = 250$ km/s.

The similar $\log(M/M_\odot)$ vs. $v_{\rm disp}$ behavior for blue and red galaxies can be considered as circumstantial evidence that the model-dependent mass-to-light ratios must be correct to some extent. The reason is that blue ($P1 < 0.25$) and red galaxies ($P1 > 0.25$) have different observed luminosi-

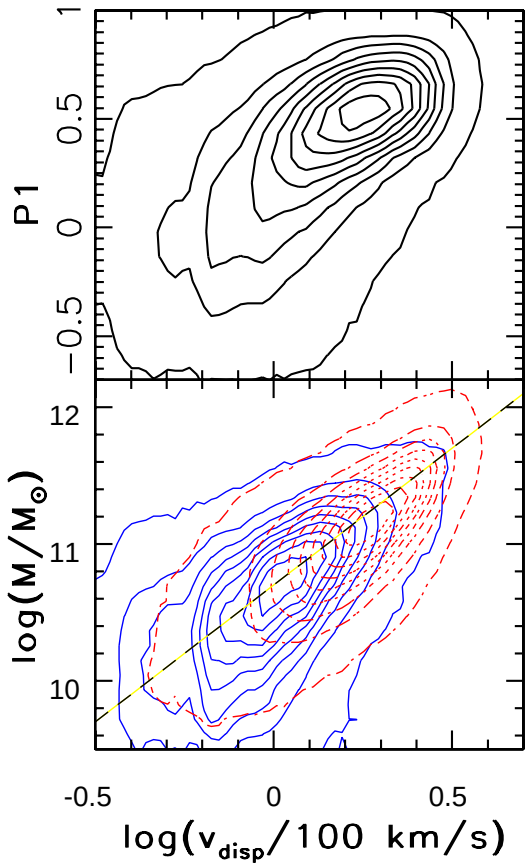

Figure 23. The top panel shows the correlation between the P1 rest-frame Strömgren color and the velocity dispersion. The bottom panel shows the correlation between the galaxy's stellar mass and the velocity dispersion, separately for galaxies with P1<0.25 (solid lines) and P1>0.25 (dashed lines). The diagonal straight line, $\log(M/M_{\odot})$=10.7+2 $\log(v_{\rm disp}/100$ km/s), is added for illustration

ties (median z band luminosity for red galaxies is larger by a factor of 2.6 than for blue galaxies), and different velocity dispersions, and only the "correct" mass-to-light ratios (medians are 1.2 and 1.9 for blue and red galaxies, respectively) will place the inferred stellar masses on the same $M - v_{\rm disp}$ relation. If the same mass-to-light ratio is used for all galaxies, the inferred mass for red galaxies would be smaller by a factor of 1.6 than for blue galaxies with the same velocity dispersion. That is, the two distributions shown in the bottom panel in Fig. 23 would be vertically offset by ∼0.2. The data constrain the offset between the two distributions to $\lesssim$0.1.

4.7 The Rest-frame Strömgren Colors vs. Red Colors

We have demonstrated in the preceding sections a good correlation between rest-frame Strömgren colors and parameters determined from the blue part of the spectrum (H_δ and $D_n(4000)$). In this section we analyze the correlation between rest-frame Strömgren colors and parameters determined from the red part of spectrum. As shown in Sec-

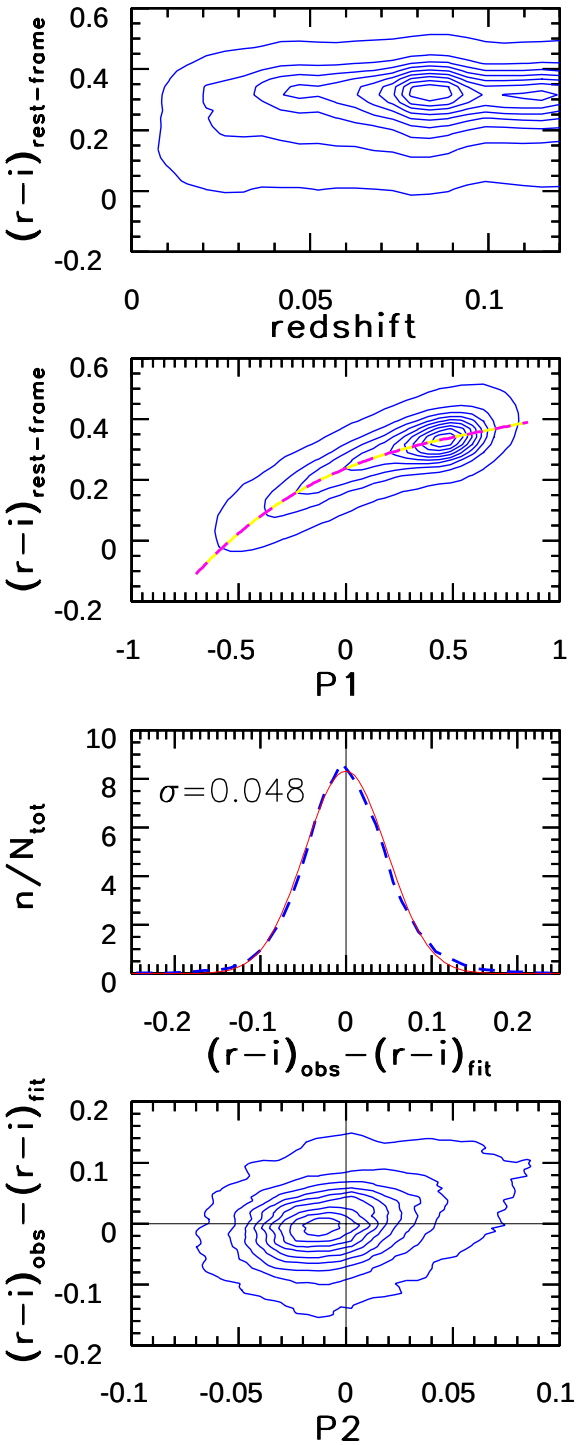

Figure 24. The top panel shows the rest-frame $r - i$ color as a function of redshift. The upper middle panel shows the correlation between the rest-frame $r-i$ color and the P1 rest-frame Strömgren color. The dashed line is a best-fit third order polynomial (see text). The distribution of residuals between the fit and measured values is shown in the lower middle panel by the thick dashed line. The thin solid line is a Gaussian with the width of 0.048 mag. The bottom panel shows the residuals as a function of the P2 rest-frame Strömgren color.

tion 3.3, the age-metallicity degeneracy cannot be broken using rest-frame Strömgren colors employed here. It is possible that additional information contained at the redder wavelengths could provide a method to separate the age and metallicity effects. If the properties of the red part of the spectrum can be fully predicted using rest-frame Strömgren colors, then such a possibility can be ruled out. Furthermore, if the blue and red parts of the spectrum are dominated by uncorrelated stellar populations, it should *not* be possible to accurately predict $r-i$ color using blue Strömgren colors.

To characterize the red part of the spectrum, we synthesize the *rest-frame* $r-i$ color, using the same method as for synthesizing rest-frame Strömgren colors. The top panel in Fig. 24 shows the rest-frame $r-i$ color as a function of redshift. Reassuringly, there is no strong dependence on redshift – the upper limit on the change of the median color with redshift is ∼0.02 mag (in the 0.02–0.12 redshift range). The correlation between the rest-frame $r-i$ color and the $P1$ color is shown in the upper middle panel. The dashed line is a best-fit

$$r-i = 0.109\,P1^3 - 0.221\,P1^2 + 0.288\,P1 + 0.238, \qquad (12)$$

which predicts the rest-frame $r-i$ color with an rms of only ∼0.05 mag. The distribution of residuals is shown in the lower middle panel, and is well described by a Gaussian distribution.

Since $P2$ is a measure of dust reddening in a galaxy, some correlation between the $r-i$ residuals and $P2$ could be expected, although the errors in the determination of $P1$, $P2$ and $r-i$, which are comparable to the magnitude of $r-i$ residuals, may easily mask it. The dependence of residuals on the $P2$ color, shown in the bottom panel, gives a hint of such a correlation. For example, the median $r-i$ residual is 0.03 mag for $P2$=0.05, while it is -0.02 mag for $P2$=-0.05.

This one-dimensional parameterization of galaxy spectral energy distributions (SEDs) extends to even longer wavelengths. Obrić et al. (2004, 2006) find that SDSS imaging magnitudes in the u and r bands, together with redshift information, can be used to predict 2MASS K band (2.2 μm) magnitudes with an rms scatter of only ∼0.2 mag, with a significant fraction of this scatter contributed by measurement errors (they estimate that astrophysical scatter is much smaller than 0.1 mag). In summary, *the UV to IR SEDs of galaxies can be described as a single-parameter family with an accuracy of 0.1 mag, or better; in addition, the more detailed spectral diagnostic parameters, such as line strengths, appear well correlated with the overall SED.*

5 THE CORRELATION BETWEEN THE REST-FRAME STRÖMGREN COLORS AND SPECTRAL EIGENCOEFFICIENTS

In the previous Section we discussed correlations between the rest-frame Strömgren colors and various other spectral parameters. Here we study the correspondence between a classification scheme based on spectral eigencoefficients proposed by Yip et al. (2004) and the principal colors P1 and P2.

Yip et al. used the Karhunen-Loéve transform to classify 170,000 SDSS galaxy spectra. These spectra are classified in a plane spanned by the mixing angles between the first three eigencoefficients, Φ_{KL} and Θ_{KL}. This classification discriminates between early-, late-type and extreme emission line galaxies (see their Section 5 for details). Given correlations between various spectral parameters discussed here, it is expected that the distribution of galaxies in the Φ_{KL}–Θ_{KL} plane is, at least to some extent, correlated with the principal colors P1 and P2.

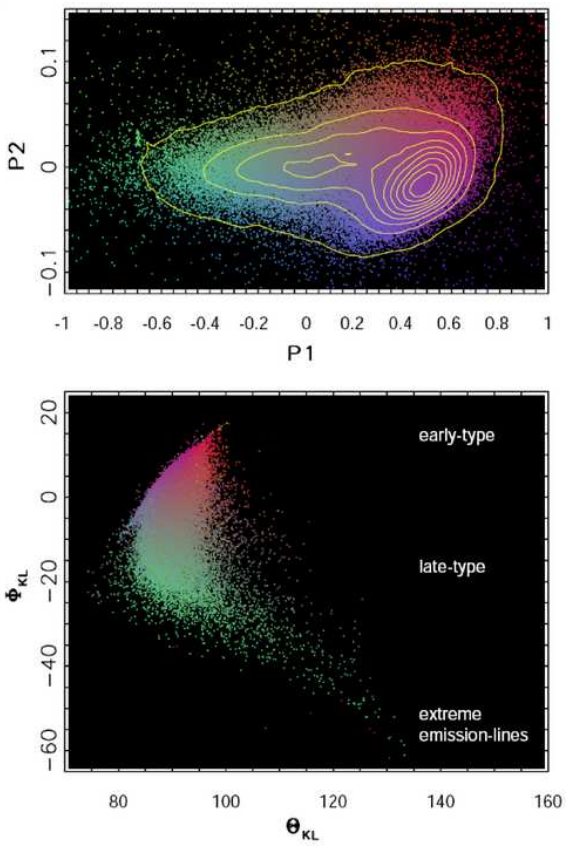

Figure 25. The bottom panel shows a spectral classification plane for galaxies proposed by Yip et al. (2004). Each galaxy is represented by a dot color-coded according to its position in the P1-P2 plane, shown in the top panel. The sequence from early-type to extreme emission line galaxies adopted from Yip et al. (2004) is shown on the right side in the bottom panel. Note the good correspondence between P1 and P2 colors and the Yip et al. classification.

Fig. 25 shows this distribution, color coded according to the position of each galaxy in the P1-P2 plane. The correlation between the P1 color and the proposed classification is evident. As discussed in detail by Yip et al., the mean spectra for galaxies selected from small (Φ_{KL}, Θ_{KL}) regions correspond to different spectral types. This suggests that the P1 color is a robust measure of galaxy type, and confirms that most of the variance in galaxy SEDs is captured by a small number of eigencomponents, as found by Yip et al.

The correlation with P2 is not as strong as for P1, but appears discernible for early- to late-type galaxies. There is a slight gradient from purple ($P2 < 0$) to red-orange ($P2 > 0$) in the $80 < \Theta_{KL} < 100$ range.

6 THE REST-FRAME UV COLORS OF $z \gtrsim 0.18$ GALAXIES

Our analysis of the rest-frame Strömgren colors in the preceeding sections did not utilize the uz magnitudes. Since the SDSS spectra cover only wavelengths longer than 3800 $\AA$, the uz magnitudes can be synthesized only for galaxies at redshifts greater than $z \sim 0.18$ (hereafter "high-z" sample). The "high-z" sample includes only $\sim 9\%$ of the 99,088 galaxies from the "main" galaxy sample, and is strongly biased towards red galaxies because of the severe luminosity cut (see Fig. 21). Nevertheless, it includes a sufficient number of blue galaxies to demonstrate a correlation between the $uz - vz$ color and the P1 color, shown in Fig. 26.

The best-fit relation shown in Fig. 26,

$$uz - vz = 0.60\, P1 + 0.77, \qquad (13)$$

can be used to "predict" the $uz - vz$ color with a residual scatter of only 0.08 mag! It is noteworthy that the $uz - vz$ residuals are not correlated with the P2 color. This small scatter means that either the dependence of the $uz - vz$ color on metallicity is not as strong as assumed a priori, or that age and metallicity for galaxies are combined in such a degenerate way that the distribution of galaxies in the $uz - vz$ vs. P1 plane is essentially one-dimensional (within this 0.08 mag scatter), similarly to their distribution in the P1 vs. P2 plane.

In order to distinguish between these two possibilities, we resort again to the Bruzual & Charlot population synthesis models (see Section 3.3). Fig. 27 shows model predictions for the dependence of the $uz - vz$ color on age and metallicity. At least for the smallest ($\lesssim$30 Myr) and largest ($\gtrsim$2 Gyr) ages, the $uz - vz$ color appears sensitive to metallicity. However, this "high-z" sample doesn't include extremely blue galaxies with implied ages below 30 Myr, or P1<-0.5 (see Fig. 8), so model predictions are not at odds with the correlation displayed in Fig. 26. The situation is less clear for old red ($\gtrsim$2 Gyr, or P1$\gtrsim$0.2) galaxies. Model tracks for 10 Gyr old galaxies (P1>0.4) predict a >0.2-0.3 mag wide range of $uz - vz$ colors, while the observed distribution has the root-mean-square scatter of 0.08 mag.

The resolution of this discrepancy is the degenerate dependence of the P1 and $uz - vz$ colors on age and metallicity. For galaxies older than $\sim$2 Gyr, *both* colors become redder as age and metallicity increase, by about the same amount. As shown in Fig. 28, for P1>0.4 the model tracks converge and become a single track irrespective of metallicity. Taken at face value, this convergence suggests that the $uz - vz$ color scatter of elliptical galaxies (at a given P1) is due to age spread, and not due to a finite width of their metallicity distribution.

This interpretation has to be taken with caution because models never produce sufficiently red $uz - vz$ colors to explain the observations of the reddest galaxies. While one is tempted to invoke the dust (which is not incorporated in these models) as an explanation of this discrepancy, these galaxies are the reddest and most luminous galaxies which are not supposed to have significant amounts of dust. Furthermore, the models show significantly different behavior for blue galaxies than displayed by the data distribution. It is quite plausible that model spectra in the rest-frame UV wavelength range require significant improvements. For example, Fig. 28 indicates that a model spectrum fit to $\lambda > 4000$ Å spectral range for a blue galaxy (say, P1=−0.5), will have the flux in the 3200–4000 Å wavelength range underestimated by $\sim$50% (0.5 mag). Note that this discrepancy cannot be easily attributed to dust effects (which are not accounted for in model spectra) because model spectra are redder, and not bluer, than the observed spectra.

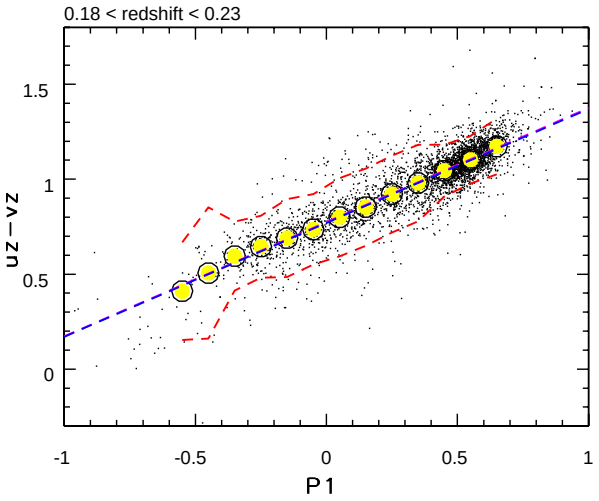

Figure 26. The $uz - vz$ color vs. P1 color-color diagram for galaxies (dots) with synthesized uz magnitudes (0.18 <z<0.23). Large circles show medians for P1 bins. The middle (straight) dashed line is the best-fit to these medians, and the other two dashed lines mark the 2σ envelope around the medians. The best-fit relation can be used to "predict" the $uz - vz$ color from P1 with a residual scatter of only 0.08 mag.

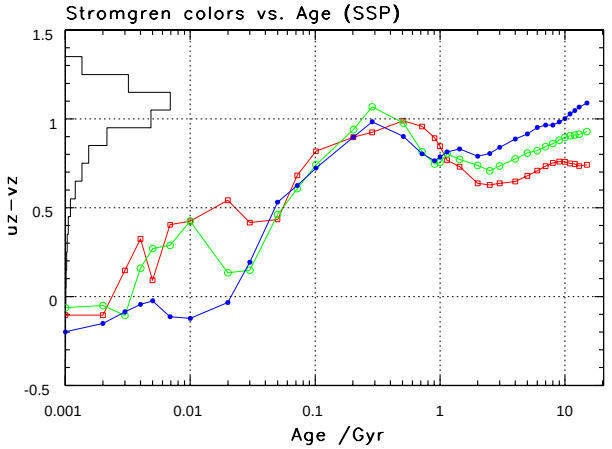

Figure 27. The Bruzual & Charlot model predictions for the dependence of the $uz - vz$ color on age and metallicity ([Z]=0.004, squares; 0.02, circles; 0.05, dots) of single stellar populations. Note that for small ages ($\lesssim$30 Myr) metallicity can have a strong impact on the $uz - vz$ color, while for intermediate ages (30 Myr $\lesssim$age $\lesssim$ 2 Gyr) it plays only a minor role. For old stellar populations ($\gtrsim$2 Gyr), the $uz - vz$ color becomes again increasingly sensitive to metallicity. However, not even for the oldest galaxies the model $uz - vz$ color is sufficiently red to explain the observations.

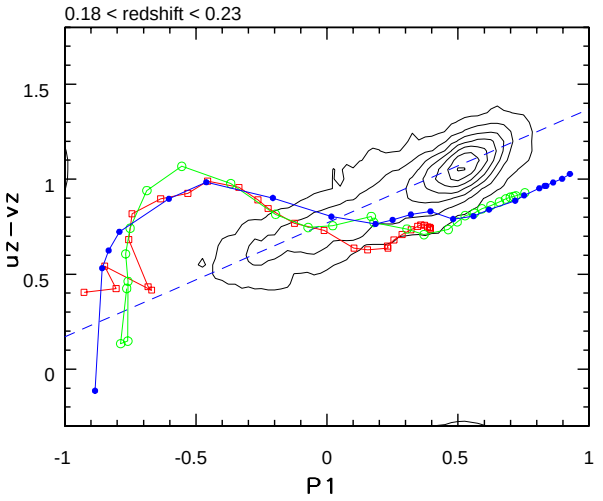

Figure 28. The $uz - vz$ color vs. P1 color-color diagram. The observed galaxy distribution is shown by linearly spaced contours (the same distribution is shown by dots in Fig. 26). The Bruzual & Charlot model predictions are shown by lines and symbols, analogously to Fig. 27. The position along each model track is controlled by the age of a single stellar population, while different tracks correspond to different metallicities. Note that the effects of age and metallicity are largely degenerate such that different model tracks do not deviate from each other by more than ∼0.1 mag. Note also the discrepancy between the model tracks and the observed distribution.

7 DISCUSSION AND CONCLUSIONS

We analyzed the synthesized rest-frame Strömgren colors for ∼100,000 SDSS galaxies. This narrow-band photometric system is well suited for studying galaxy colors in the 4000–5800 Å wavelength range. Galaxies form a narrow locus in the rest-frame Strömgren $bz - yz$ vs. $vz - yz$ color-color diagram, with a width of only 0.03 mag. This small width, in addition to demonstrating that the errors in synthesized colors are small, shows that the slope of galaxy spectra in the 3200–5800 Å wavelength range is practically a one-parameter family. This conclusion is independent of the details of the employed photometric system.

Using the Bruzual & Charlot population synthesis models, we find that the dependence on age and metallicity is *fully absorbed* in the first principal color axis, $P1$. This color is essentially a measure of the Hubble type (in sense of early vs. late type galaxies, rather than detailed morphological classification). It is not possible to break the age-metallicity degeneracy with any of the observables discussed here. This may not be possible even when using standard methods such as Lick indices, at least in the case of elliptical galaxies (Eisenstein et al. 2003). As demonstrated by Eisenstein et al., the strengths of numerous metal lines, such as Mg b, can be accurately predicted from the strength of the H_δ line (see their Fig. 5); hence, no additional information can be extracted from the measurements of those lines. On the other hand, Tremonti et al. (2004) report a very tight mass-metallicity relation (0.1 dex scatter in metallicity at a given mass) for ∼50,000 SDSS star-forming galaxies. Thus, it may be that age and metallicity are strongly correlated, too, which then would provide a trivial solution to the problem of breaking the age-metallicity degeneracy. Indeed, such a relation has been claimed for disk stars in our Galaxy (Twarog 1980; however, see also Feltzing, Holmberg & Hurley 2001).

The second principal color axis, $P2$, is independent of stellar age and metallicity, at least according to the Bruzual & Charlot models. We stress that the definition of this color is purely *observational*, and the models explain both its value and narrow distribution width. The $P2$ distribution width (0.03 mag) measured using SDSS data is smaller than typical observational errors in rest-frame colors using other data available to date ($\gtrsim$0.05 mag). The $P2$ color appears most sensitive to the galaxy dust content, as demonstrated by the analysis of model-dependent estimates of the dust content by Kauffmann et al. (2003a), and also by the redder $P2$ colors for galaxies detected by the IRAS survey. Of course, $P2$ could be *indirectly* related to metallicity, if the dust content depends on metallicity (that is, the observed $P2$ color could be correlated with metallicity as a result of radiative transfer through interstellar dust, rather than due to the dependence of the source function on metallicity).

The principal colors are well correlated with numerous other spectral parameters determined from bluer and redder spectral ranges, as well as with the position of a galaxy in the BPT diagram constructed with emission-line strength ratios. These good correlations suggest that not only are the overall UV-IR SEDs a nearly one-parameter family, but that the same parameter also controls the properties of emission lines. Most notably, there is a good correspondence between the stellar mass-to-light ratio estimates by Kauffmann et al. (2003a) and the principal color $P1$.

The low dimensionality of galaxy spectra implied by the numerous correlations among the continuum and spectral parameters shown here is in good agreement with the conclusions by Yip et al. (2004), who applied the principal component analysis to SDSS galaxy spectra. The same conclusion was reached in a detailed study of elliptical galaxies by Eisenstein et al. (2003). These conclusions are valid for the overwhelming majority of all galaxies; however, we emphasize that the analysis presented here is based on low-order statistical moments (such as root-mean-square scatter) and cannot rule out a possibility that as many as 5-10% of galaxies behave differently.

Our results support the suggestion by Rakos and collaborators (Fiala, Rakos & Stockton 1986) that the rest-frame Strömgren photometry provides an efficient tool for studying faint cluster galaxies and low surface brightness objects, without the need for time-consuming spectroscopy. For example, the stellar mass-to-light ratio can be determined from $P1$ with an rms scatter of only 0.10. Since the brightest cluster galaxies can be selected from SDSS data to redshifts of ∼0.8 (e.g. Ivezić et al. 2002), this method can be used to quantify the rise in star formation activity with cosmic epoch, and the Butcher-Oemler effect, with an unprecedented accuracy. We are currently undertaking such an observational program.

ACKNOWLEDGMENTS

V.S. and Ž.I. are thankful to the Princeton University for generous financial support. We thank Ching-Wa Yip for pro-

viding us galaxy classification results, and for useful discussions.

Funding for the SDSS and SDSS-II has been provided by the Alfred P. Sloan Foundation, the Participating Institutions, the National Science Foundation, the U.S. Department of Energy, the National Aeronautics and Space Administration, the Japanese Monbukagakusho, the Max Planck Society, and the Higher Education Funding Council for England. The SDSS Web Site is http://www.sdss.org/.

The SDSS is managed by the Astrophysical Research Consortium for the Participating Institutions. The Participating Institutions are the American Museum of Natural History, Astrophysical Institute Potsdam, University of Basel, Cambridge University, Case Western Reserve University, University of Chicago, Drexel University, Fermilab, the Institute for Advanced Study, the Japan Participation Group, Johns Hopkins University, the Joint Institute for Nuclear Astrophysics, the Kavli Institute for Particle Astrophysics and Cosmology, the Korean Scientist Group, the Chinese Academy of Sciences (LAMOST), Los Alamos National Laboratory, the Max-Planck-Institute for Astronomy (MPA), the Max-Planck-Institute for Astrophysics (MPIA), New Mexico State University, Ohio State University, University of Pittsburgh, University of Portsmouth, Princeton University, the United States Naval Observatory, and the University of Washington.

REFERENCES

Abazajian, K., Adelman, J.K., Agueros, M., et al. 2003, AJ, 126, 2081
Baldry, I.K, Glazebrook, K., Brinkmann, J., et al. 2004, ApJ, 600, 681
Baldwin, J., Phillips, M., and Terlevich, R. 1981, PASP, 93, 5
Bell, E.F., McIntosh, D.H., Katz, N. & Weinberg, M.D. 2003, ApJ, 585, L117
Bernardi, M., Sheth, R.K., Annis, J., et al. 2003a, AJ, 125, 1817
Bernardi, M., Sheth, R.K., Annis, J., et al. 2003b, AJ, 125, 1849
Bernardi, M., Sheth, R.K., Annis, J., et al. 2003c, AJ, 125, 1866
Bernardi, M., Sheth, R.K., Annis, J., et al. 2003d, AJ, 125, 1882
Blanton, M.R., Dalcanton, J., Eisenstein, D., et al. 2001, AJ, 121, 2358
Blanton, M.R., Hogg, D.W., Bahcall, N.A., et al. 2003, ApJ, 592, 819
Blanton, M.R., Hogg, D.W., Bahcall, N.A., et al. 2003, ApJ, 594, 186
Bruzual, A.G. & Charlot, S. 1993, ApJ, 405, 538
Bruzual, A.G. & Charlot, S. 2003, MNRAS, 344, 1000
Eisenstein, D.J., Hogg, D.W., Fukugita, M., et al. 2002, ApJ, 585, 694
Feltzing, S., Holmberg, J. & Hurley, J.R. 2001, A&A, 377, 911
Fiala, N., Rakos, K.D. & Stockton, A. 1986, PASP, 98, 70
Hauck, B. & Mermilliod, M. 1998, A&AS, 129, 431
Heckman, T.M., Kauffmann, G., Brinchmann, J., et al. 2004, ApJ, 613, 109
Hao, L., Strauss, M.A., Tremonti, C., et al. 2005a, AJ, 129, 1783
Hao, L., Strauss, M.A., Tremonti, C., et al. 2005b, AJ, 129, 1795
Hopkins, A.M., Miller, C.J., Nichol, R.C., et al. 2003, ApJ, 599, 971
Ivezić Ž., Menou, K., Knapp, G.R., et al. 2002, AJ, 124, 2364
Ivezić, Ž., Lupton, R.H., Anderson, S., et al. 2003, Proceedings of the Workshop *Variability with Wide Field Imagers*, Mem. Soc. Ast. It., 74, 978 (also astro-ph/0301400)
Kauffmann, G., Heckman, T.M., White, S.D.M., et al. 2003a, MNRAS, 341, 33
Kauffmann, G., Heckman, T.M., White, S.D.M., et al. 2003b, MNRAS, 341, 54
Kauffmann, G., Heckman, T.M., Tremonty, C., et al. 2003c, MNRAS, 346, 1055
Kennicutt, R.C. 1998, ApJ, 498, 541
Kewley, L., Jansen, R.A. & Geller, M.J. 2005, PASP 117, 227
Lupton, R.H., Ivezić, Ž., Gunn, J.E., Knapp, G.R., Strauss, M.A. & Yasuda, N. 2002, in "Survey and Other Telescope Technologies and Discoveries", Tyson, J.A. & Wolff, S., eds. Proceedings of the SPIE, 4836, 350
Obrić, M., Ivezić, Ž., Best, P.N., et al. 2006, submitted to MNRAS
Obrić, M., Ivezić, Ž., Kauffmann, G., et al. 2004, IAUS, 222, 533 (also astro-ph/0404503)
Odell, A.P., Schombert, J.M. & Rakos, K.D. 2002, AJ, 124, 3061
Oke, J.B. & Gunn, J.E. 1983, ApJ, 266, 713
Petrosian, V., 1976, AJ, 209, L1
Rakos, K.D. & Dominis, D. & Steindling, S. 2001, A&A, 369, 750
Rakos, K.D. & Schombert, J.M. 1995, ApJ, 439, 47
Rakos, K.D. & Schombert, J.M. 2004, AJ, 127, 1502
Sheth, R.K., Bernardi, M., Schechter, P.L., et al. 2003, ApJ, 594, 225
Shimasaku, K., Fukugita, M., Doi, M., et al. 2001, AJ, 122, 1238
Spergel, D.N., Verde, L., Peiris, H.V., et al. 2003, ApJS, 148, 175
Stoughton, C., Lupton, R.H., Bernardi, M., et al. 2002, AJ, 123, 485
Strateva, I., Ivezić, Ž., Knapp, G.R., et al. 2001, AJ, 122, 1861
Strauss, M.A., Weinberg, D.H., Lupton, R.H., et al. 2002, AJ, 124, 1810
Tremonti, C., Heckman, T.M., Kauffmann, G., 2004, ApJ, 613, 898
Twarog, B.A. 1980, ApJ, 242, 242
Vanden Berk, D.E., Wilhite, B.C., Kron, R.G., et al. 2004, ApJ, 601, 692
Yip, C.W., Connolly, A.J., Szalay, A., et al. 2004, AJ, 128, 585
York, D.G., Adelman, J., Anderson, S., et al. 2000, AJ, 120, 1579
Zakamska, N.L., Strauss, M.A., Krolik, J.H., et al. 2003, AJ, 126, 2125
Zakamska, N.L., Strauss, M.A., Heckman, T.M., Ivezić Ž., & Krolik, J.H. 2004, AJ, 128, 1002